CHAPTER 1. INTRODUCTION

1.1. Industrial objective

The main objective in developing the new armoured steel plate to supersede the currently used steel A and steel B plates, is the manufacture of lighter armoured vehicles by decreasing the required thickness of the steel plates. The new plate should be able to withstand a 5.56 mm R4 round whereas the steel A and steel B plates manufactured currently, need a 8.5 to 20 mm thickness or higher for this ballistic requirement. According to ISCOR [1], the properties listed in Table 1.1 would need to be achieved to meet this objective.

Table 1.1 Specifications for the new armoured steel plate [1]

Property	Specification
Brinell hardness	570-640 BHN
Charpy V-notch transverse impact energy on full size specimens [2]	12 Joules (minimum) at $-40\,^{0}C$
Yield strength R_p at 0.2%	1500 MPa (minimum)
Ultimate tensile strength	2000 MPa (minimum)
Elongation of a 50 mm gauge length	7% (minimum)

The process parameters for the new armoured steel plate should be as close as possible to the existing ones for the current steels A and B produced by Mittal Steel South Africa. The processing parameters during hot rolling are more or less fixed, although the post-rolling heat treatment temperatures and times can be slightly adjusted. After preliminary austenitisation of the current steel B, followed by water quenching and a low-temperature tempering, it appears that the harder new armour plate will almost certainly require a change in composition for its higher hardness requirement (Carbon content) and hardenability (Carbon and alloying elements), as well as for its toughness requirement.

To move from the current steel B to the new armour plate, will require an improvement of ballistic properties through optimising the plate's resistance to *impact* or *shock* loading and its resistance to *spalling* as well as meeting the resistance against *localised yielding* and *ballistic perforation*. Minimum *hardness* and *strength* requirements of the alloy should also be realised. The design of the steel alloy and its heat treatment should allow an efficient way for the development and manufacture of the armoured steel plate (steel making, rolling and heat treatment parameters). The assessment of the ballistic performance will be provided after ballistic testing according to the military and civil specifications for South Africa as determined by ARMSCOR. These standardised specifications for ballistic tests in South Africa are presented in Table 1.2. Each test consists of at least five firings of rounds under the prescribed conditions.

Table 1.2: Specification for the assessment of armour plate materials in South Africa [1]

Obliquity	0^0
Muzzle velocity	930 m/s (minimum)
Distance	30 m maximum
Assessment	1. No light path going through the thickness of the plate in the impact region (i.e. no visible through-penetration) 2. No spalling at the rear face of the plate after ballistic testing

1.2. Project aim and methodology

The research project was undertaken with the aim of developing an improved understanding of the relationship between ballistic properties of martensitic armour plate steels and their structures and mechanical properties. By this means design criteria have been proposed that meet the industrial objective outlined in Section 1.1. In the course of the project, benchmarking was carried out using the scientific and industrial background on armour steels currently produced or used in South Africa and throughout the world. Microstructural investigations were used to explain the high or the low ballistic performance of these steels before designing the candidates for the advanced performance RB600. Mechanical testing, fracture analysis, measurement of martensite start temperatures by dilatometry, phase analysis by X-ray diffraction, characterisation of the martensite and surface relief analysis and ballistic tests were conducted to explain the differences in performances and to optimise the ballistic as well as the mechanical properties of the new martensitic armour steels through the control of the chemical composition and the heat treatment parameters.

CHAPTER 2. LITERATURE REVIEW

2.1 Industrial background

Mittal Steel South Africa already manufactures both the steels A and B at its Vanderbijlpark plant that require armour resistance. These steels are used typically in combat vehicles, security vehicles, bulletproof jackets and security doors. The specifications for the chemical compositions of the current armour steels A and B are listed in Table (2.1). From this table, it appears that the compositions for the two products differ mainly in their Nickel and Chromium contents. The ratio of their Nickel to Chromium content are respectively 2 and 0.7 for the respective steels A and B. Steels A and B are fully killed fine-grained steels, which are also calcium treated and vacuum degassed to achieve low sulphur levels and inclusion content. These armour plate steels are quenched and tempered to achieve an ultra high strength with a fine microstructure.

Table (2.1). Specifications for the chemical compositions of the currently produced armour steels A and B

	%C	%Mn	%P	%S	%Si	%Cu	%Ni	%Cr	%Mo
Steel A: specification	0.29-0.31	0.80-0.90	0.0-0.01	0.0-0.003	0.15-0.25	0.0-0.03	2.8-3.0	0.8-1.0	0.45-0.55
Steel A: actual composition	0.317	0.855	0.008	0.002	0.176	0.026	2.8	0.79	0.45
Steel B: specification	0.30-0.32	0.55-0.65	0.0-0.015	0.0-0.005	0.30-0.45	0.0-0.03	1.4-1.5	1.5-1.6	0.55-0.60
Steel B: actual composition	0.253	0.606	0.007	0.002	0.327	0.012	1.41	1.54	0.58

2.1.1. The heat treatment cycle of steel A.

The Brinell hardness range for steel A is:

Table (2.2). Brinell hardness range of steel A armour plate [1]

Thickness [mm]	Brinell hardness
3.5 to 8	460 to 540 BHN
10 to 25	380 to 440 BHN

The typical heat treatment cycle of steel A consists of [1]:

Table (2.3): Typical heat treatment of steel A

Plate Thickness [mm]	Austenitisation temperature [^{0}C]	Austenitisation time [minutes]	Tempering temperature [^{0}C]	Tempering time [minutes]
6	900	20	280	38
8	870	24	400	46

The 3.5 to 4.5mm steel A plates are heated and then quenched in a water-cooled press. Plates from 6 mm to 25 mm thick are heat-treated in a roller quenching plant that subjects the entire plate to a rapid high volume water quench after solution treatment.

The high cooling rate ensures maximum use of the alloying elements to give the required properties throughout the plate thickness [3]. After quenching, plates are tempered in a tempering furnace where the temperature is selected so that the desired degree of hardness for the specific plate thickness is obtained. The 3.5 to 4.5mm steel A plates are not tempered after quenching but are used in the as-quenched condition[1].

2.1.2. The heat treatment cycle of the steel B

The thermomechanical treatment for steel B consists of:

1. Hot rolling in the austenite region (above A_{c3}) to the final thickness;
2. Stack the plates on top of each other for a slow cool to remove possible Hydrogen cracking;
3. Send the cold plates to the Roller Quenching plant;
4. Solution treatment at 910°C;
5. Water quenching in the Roller Quenching plant (for the 3.5 to 4.5 mm plates); and
6. Low temperature tempering.

The steel B Brinell hardness' range is given in Table (2.4).

Table (2.4): Brinell hardness range of steel B Plates

Thickness [mm]	Brinell hardness
6 to 12	477-532 BHN
15 to 25	450-512 BHN

The results after ballistic testing must conform to the ARMSCOR-ARMOUR PLATE SPECIFICATION FOR RSA, specification No. SK112.

- **Storage**: all material, with exception of the 3.5 to 4.5 mm plates, are shot blasted after heat treatment to remove surface scale. The material must preferably be stored under roof to prevent corrosion.

- **Fabrication** [1] :
    1. The hardness, high strength and toughness, as well as the weldability are the main considerations for fabrication of steels A and B;
    2. Due to the high hardness of the materials, bending is not recommended. However, if any form of bending is to be done, it is advised that it be done transverse to the rolling direction and at room temperature of $\pm 25^{0}$C. Cut edges should be smoothly ground before bending.
    3. Hot rolling: local or general heating must be performed before the final heat treatment, as this could have an effect on the properties of the material. The exposed face of the armour plate on the vehicle can have a higher hardness than the opposite face facing into the vehicle. The latter must have a higher strength.

4. Machining can be performed using high-speed tool steel tips and reducing the speed to 50% of speeds used for normal carbon steels.
5. Flame cutting is not recommended for plate thickness less than 15 mm. For these thicknesses plasma or laser cutting is recommended.
6. Preheating and welding: Preheating usually plays an important role in the application of armour steel plates. Accordingly, a welding specification SK108 has been developed for the correct welding procedures for steels A and B [1] . Preheating of plates is recommended to minimize the adverse effect of welding and flame cutting on the microstructure of the heat-affected-zone (HAZ) by reducing the cooling rate in the HAZ. Rapid cooling after welding and flame cutting result in a hard and brittle martensitic microstructure, which is susceptible to hydrogen cracking. The recommended maximum preheating temperature is 120^{0}C [1].

Direct-quenching and tempering after hot rolling is now a viable technology in the production of high strength steel plate, and it is widely practiced, especially in Japan.

In conventional reheat-quenching and tempering, microstructures and properties are determined by the chemical composition and the tempering conditions. Direct-quenching is an alternative route to reheat-quenching as practised at the Vanderbijlpark plant of Mittal Steel (South Africa)[4].

2.2 Scientific background

2.2.1. Ballistic material

Each class of armour plate is heat treated to provide maximum resistance to ballistic perforation. The microstructure must be homogeneous throughout the section thickness and without inclusions that would act as crack initiators.

The external surface can present a higher hardness for resistance against penetration and compressive impact, whereas the internal surface could have a higher tensile strength [2]. Cast armour has always been more resistant ballistically than rolled armour due mainly to the fundamental difference in mechanical and metallurgical properties between rolled and cast steel [2]. However production of armour plate is not feasible in cast forms.

It is possible to design a casting with smoother contours and higher obliquities than a flat plate, although normally heavier than a corresponding structure fabricated from rolled plate and in many cases with equal or even improved ballistic protection. Cast homogeneous steel armour is still used on Army Combat Vehicles under MIL-S-11356 to produce such components as hulls, turrets, cupolas, hatch covers, etc.

A large amount of empirical data obtained from a variety of tests confirmed that the armour strength or hardness of the steel is a very important parameter in resisting ballistic penetration. According to this design philosophy the candidate armour material should exceed the hardness of the projectile [2]. This can be achieved primarily by thermal or thermomechanical processing.

The assessment criterion of ballistic resistance is that of “no visible light to pass through the impacted plate after the test” as illustrated by Figure 2.1 and quoted from [2].

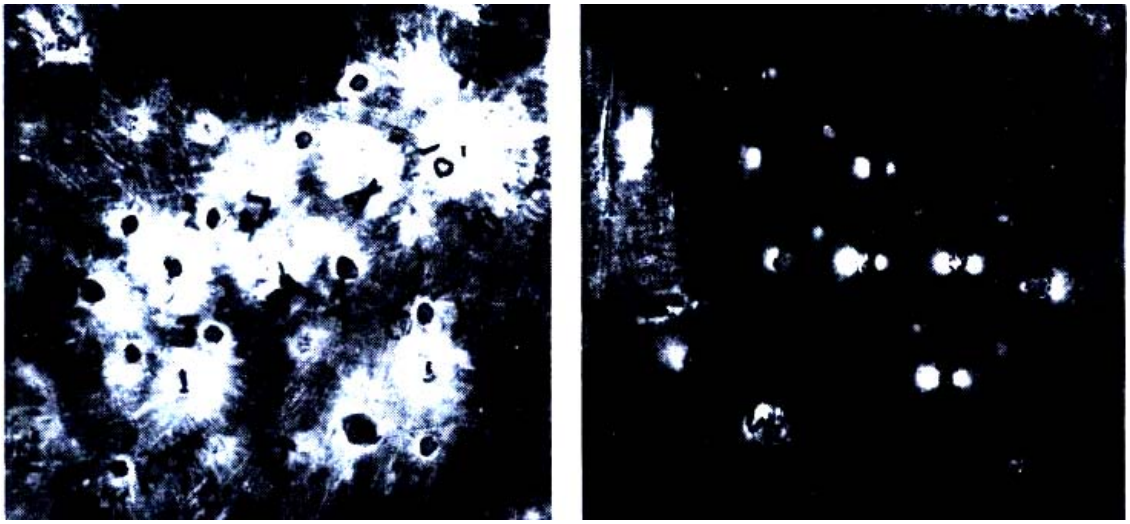

(a) FRONT (b) REAR

Figure.2.1 (a) and (b), Multiple ballistic impact capability of armour plate made from an unidirectionally solidified ingot at a hardness in excess of 55 HRC. Light spots show the difference in sizes between the openings in the front and the rear faces of the impacted plate.

The following figure shows the increase in the ballistic performance versus hardness as a function of technological developments.

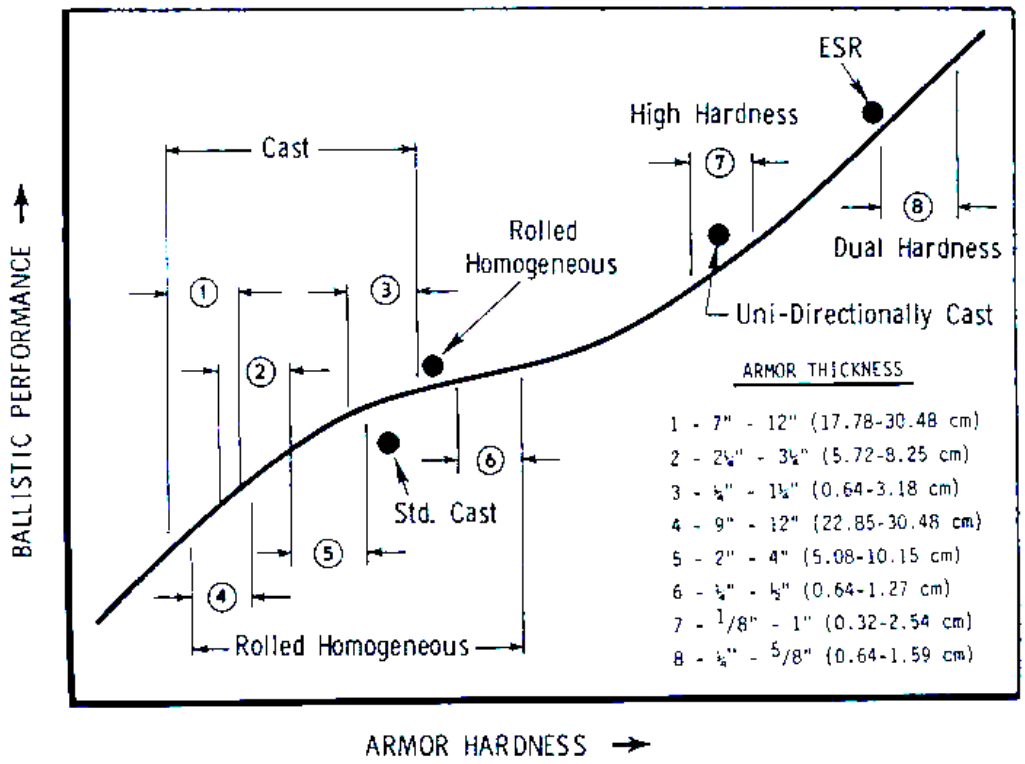

Figure.2.2. Relationship between armour hardness and ballistic performance [2]

There are several additional factors to consider in the choice of alloy for armour plate but the major consideration would be that it should be effective in the field, and it should be light, which in turn gives a variety of advantageous secondary effects.

Above all the armour plate must also be cost-effective. Other considerations are that the armour plate should be amenable to modern fabrication and construction techniques and be readily weldable and capable of being produced in a variety of shapes. Bulk is an important factor because if the armour is bulky even though its area density is low, it will be difficult to provide sufficient room under the armour to meet volume requirements for the crew, gun, ammunition, fuel and power train, etc. For many years various alloy steels have measured up to this requirement very well. Armour application for these steels is well understood and can be made with optimisation of various properties by changing the proportion and presence of the alloying elements.

Although steel is a dense material with a larger area density (i.e. mass per unit area) comparatively to other armour materials, it does offer very good levels of protection against KE (Kinetic Energy) and HESH (Highly Explosive Squash Head) attacks, but its performance against HEAT (Highly Explosive Anti Tank) attack is considerably reduced [2]. Most alloy steels contain some or all of the elements Manganese, Chrome, Nickel, Molybdenum and Vanadium to give the correct blend of high strength and resistance to fracture or toughness.

The major problem with all armour is that if the energy from the projectile is not to be transferred from the armour to the supporting structure then a way has to be found to dissipate the energy before this happens or the secondary effect may be equally fatal.

Experience indicates that homogeneous steel armour (i.e. not a layered combination made from layers of different steels) should be made as hard as possible for defeating small arms and armour piercing (AP) ammunition. However, as homogeneous steel becomes harder it also becomes more brittle and as the material becomes more brittle, its ballistic limit cannot be measured due to severe fracture of the armour. Thus, limits on homogeneous armour hardness have to be established to prevent shatter of the armour due to embrittlement, but not necessarily because of strength limitations on the ballistic limit. This important fact has formed the basic guideline for improved steel armour development programs. That is, to increase the steel armour's ballistic limits by increasing its hardness without increasing the tendency towards brittle failure. An armour hardness of at least 58 to 62 Rockwell C would be required to induce shattering of the projectile upon impact [2]. Various definitions for complete and partial penetration are illustrated in Figure 2.3.

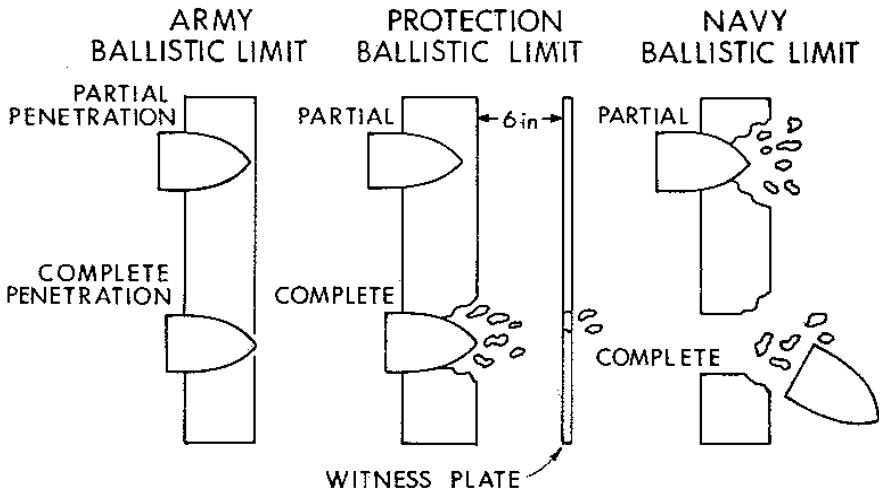

Figure 2.3. Definitions of perforation and partial penetration for defining the ballistic limit

The ballistic superiority of steels of higher metallurgical quality has been demonstrated often. The development of unidirectionally solidified wrought steel armour showed that cast steels with superior ductility could be produced by unidirectional solidification, which produces a cast structure in which columnar grains extend from the chill surface completely through the casting. The resulting solidified steel ingots have been found to be virtually free of gross porosity and with a much finer segregation pattern, factors that contribute to higher ductility [2].

The homogenisation heat treatment, which consists of holding the casting at 1316°C for 64 hours, would virtually eliminate alloy segregation. Steels of armour composition have been produced by this process and have been homogenised, rolled, and heat-treated to hardness levels ranging from 50 to 60 HRC.

The important requirement of structural tank armour is that it should maintain structural integrity at sub-zero temperatures when impacted by overmatching artillery rounds. Test plates are inspected after proof testing for their ability to withstand fracture, spalling, and cracking. The long-standing empirical materials specification, which applies to structural tank armour and its ability to maintain integrity at low temperatures, requires that the material must have a minimum of 27.12 J (20 ft-lbs) transverse Charpy V-notch impact energy at a temperature of -40^{0} C [1, 2].

2.2.2 Stress waves in solids

The response of materials and structures to intense impact loading is quite complex. For loading conditions that result in stresses below the yield point, materials behave elastically and Hooke's law is applicable for metals. However the mathematical solutions for various loading conditions in this regime are obtained for semi-infinite bodies. Practical impact problems involve strikers and targets with finite boundaries, which exert considerable influence on their behaviour. As the intensity of the applied load is increased, the material is deformed into the plastic range. The behaviour in this range involves large deformations together with localised heating, and often failure of the colliding solids through a variety of mechanisms. With still further increases in loading intensity, pressures are generated that exceed the strength of colliding solids by several orders of magnitude which, in effect, then start behaving hydrodynamically [5]. Failure modes in impacted plates may be classified as one of the six illustrated in Figure 2.4.

For low intensity excitations, both the geometry of the entire structure as well as the nature of the material from which it is made, play a major role in resisting any external forces. As loading increases, the response tends to become highly localized and is more affected by the constitution of the material in the vicinity of the impact region than the geometry of the structure. The description of the phenomena in terms of elastic, plastic, and shock waves becomes appropriate.

When either a dilatational or distortional wave impinges on a boundary of the solid, waves of both tensile and compressive types are generated. Of particular interest in impact situations is the normal impingement of a strong compressive pulse on a free surface. The pulse is reflected from any discontinuity or a free surface as a tensile wave and if its magnitude is greater than the tensile fracture strength of the material, fractures will occur.

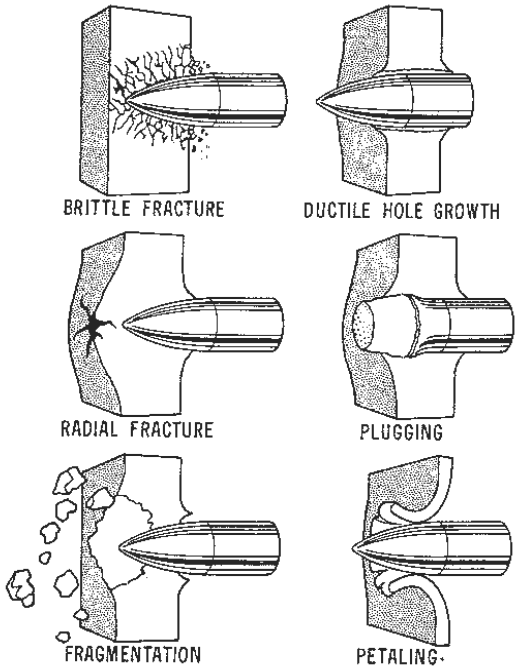

Figure 2.4. Failure modes in impacted plates [2]

Simple analyses predict reasonably well the location of the fracture plane and the size and speed of the ejected material for high strength solids. If after fracture, the magnitude of the stress pulse still exceeds the material's tensile strength, multiple fractures can occur [5]. The reflection of the input compressive pulse and the subsequent formation of a tensile wave are illustrated in Figure 2.5. The evolution of the phenomenon is depicted as different time function of the compressive wavelength λ and the celerity of the light C.

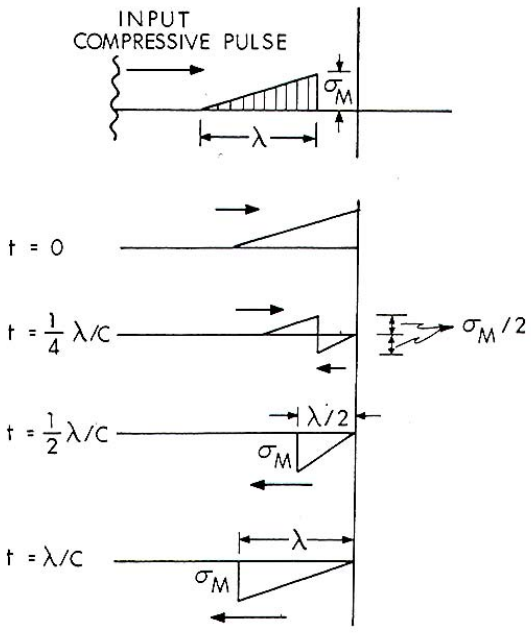

Figure 2.5: Illustration of the propagation and reflection at a free surface of the shock-induced compressive wave and its subsequent conversion into a tensile wave [2]

A high dynamic tensile strength is then required to avoid multiple fractures and spallation during ballistic testing. This observation will be compared later to the experimental results of the ballistic performances in this study on 13 armoured steels. As the intensity of the applied load increases, the material is driven beyond its elastic limit and becomes plastic. Two waves now propagate in the solid, an elastic wave (or precursor) followed by a much slower but more intense plastic wave. The principle is illustrated considering an elastic-linear hardening behaviour for a material whose Young's modulus is E, the yield strength is σ_y and the specific mass is ρ. The elastic wave front propagates at the speed $C_0 = \frac{\sqrt{E}}{\rho}$ whereas the slow plastic wave follows at a velocity $C_1 = \frac{\sqrt{E_1}}{\rho}$ where the two values of E differ because of elastic linear hardening. Figure 2.6 illustrates the delay of the plastic wave front on the elastic wave in the space-stress reference. The same principle may be illustrated in velocity-strain space as in Figure 2.7.

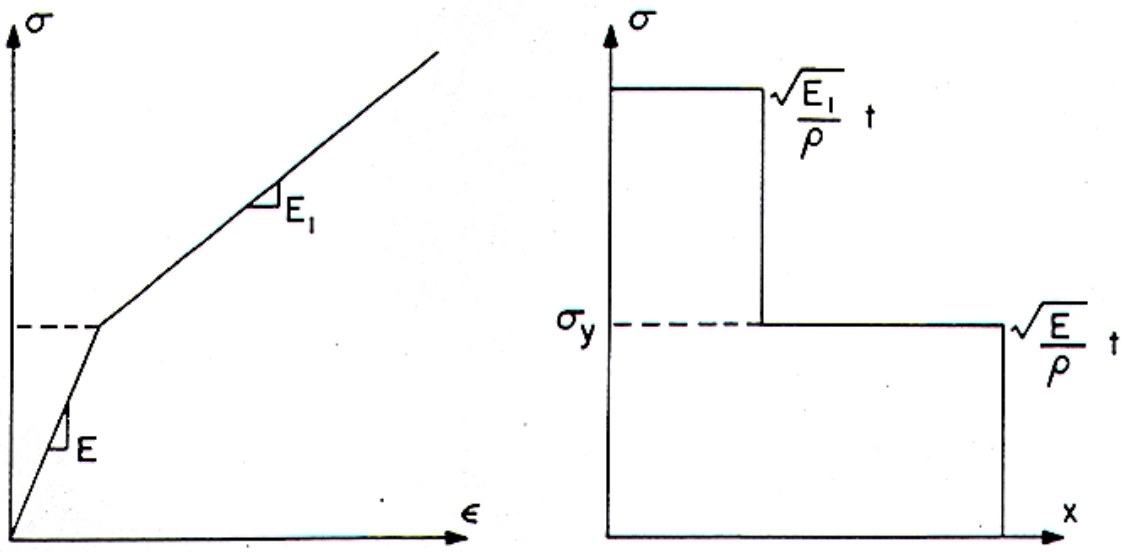

Figure 2.6: Stress-strain relationship and wave-profile for elastic-linear hardened material

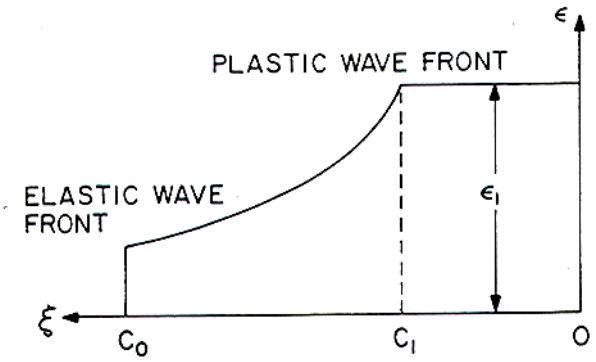

Figure 2.7: Strain distribution in a rod produced by a its constant velocity impact at end. ξ=x/t.

If the characteristics of the medium are such that the velocity of propagation of large disturbances is greater than the propagation velocity of smaller ones, the stress pulse develops a steeper and steeper front on passing through the medium, and the width of this front is ultimately determined by the molecular constitution of the medium. The shock wave (or steep pressure pulse) thus formed, differs from the high pressures generated by conventional methods in that it relies on the inertial response of the material to rapid acceleration rather than on static constraints. If the intensity of the loading is so great or its duration so short that the material no longer possesses rigidity, it will behave as though it had the properties of a fluid. Transverse (shear) waves cannot exist then within the body and only a longitudinal wave will be propagated with a velocity c given by:

$$c^2 = \frac{K}{\rho} \qquad \text{(Eq 2.2.2-1)}$$

where K is the bulk elastic modulus and ρ the density. The bulk modulus K may be found from Young's elastic modulus E and Poisson's ratio ν:

$$K = \frac{E}{3(1-2\nu)} \qquad \text{(Eq 2.2.2-2)}$$

In this shock wave regime, extremely high pressures are generated which can lead to changes in the density of materials with changes as large as 30% in steels [5]. The stress response is governed by dilation of the steel, since pressures are typically in the hundreds of kilobars while material strengths are only of the order of a few kilobars. This circumstance led to the development of hydrodynamic theories in which the material strength was neglected and the metal assumed to behave as a perfect fluid with resistance only to dilation. Lee [5] suggests that hydrodynamic theories need to be modified to account for strength effects and finite deformations. Finite strains and strength effects can play a dominant role in determining the stress-wave profile. For fracture problems, this profile is crucial for determining the location and the type of failure.

2.2.3. Material behaviour at high strain rates

The behaviour of materials at high rates of strain has been studied with considerable interest since World War II when dynamic plasticity and plastic-wave propagation first received attention. The most general form of a material-constitutive equation should cover the prediction of material behaviour under the total range of strain rates that may be encountered. However, this can be difficult even for an uniaxial stress and, therefore, the majority of constitutive equations generally cover only a narrow range of strain rates. This is consistent with the physics of the problem since different mechanisms govern the deformation behaviour of materials within different strain-rate regimes.

Five classes of strain rates are identified due to dynamic loadings in metallic structures. The duration of impact, the state of stress and strain as well as the thermal effect accompanying each class, are shown in Table 2.5. From this table it appears that at very high strain rates and the associated short time scale involved, thermodynamic

considerations become important. The nominally isothermal conditions then translate to adiabatic conditions.

Table (2.5): Classes of strain rates [5]

Strain rate [s^{-1}]	10^{-8} to 10^{-6}	10^{-2}	10^{0}	10^{2} to 10^{4}	10^{6}
Characteristic time [s]	10^{6} to 10^{4}	10^{2} to 10^{0}	10^{-2}	10^{-4} to 10^{-6}	10^{-8}
	Creep	Quasi-static	Intermediate strain rate	Bar impact	High-velocity plate impact
			Mechanical resonance in machines and specimen	Elastic-plastic wave propagation	Shock wave propagation
Isothermal			Adiabatic		
Inertia forces neglected			Inertia forces important		
Plane stress					Plane strain
Increasing stress levels →					

2.2.4. Ballistic performance

The development of metallic armour involves a large number of tedious ballistic experiments, since any change in alloy composition or heat treatment parameters significantly alters the ballistic performance. Although considerable knowledge exists on how the alloy compositions and heat treatment parameters affect the mechanical properties, a quantitative understanding of the correlation between the mechanical properties and the ballistic performance is still lacking [6]. Most of the earlier models on ballistic performance focused on the target and the projectile geometry and penetration parameters such as striking velocity and the striking angle. Contrarily most of the actual models are based on the mechanical properties of the projectile and the target, with the latter related to the metallurgical processes. Srivathsa et al [6] suggest that the kinetic energy of the projectile is absorbed in the following three modes:

1. the elastic deformation of the material;
2. the plastic deformation of the material; and
3. the kinetic energy imparted to the target material.

The total energy absorbed in each of the above cases is the product of the energy absorbed per unit volume and the participating volume. In previous work [7] the same authors suggested a model for the calculation of the energy Ψ per unit area-density (ρd) absorbed by the three modes as follows:

$$\frac{\Psi}{\rho d} = \pi t^2 v_r^4 \left[\frac{\alpha_I}{2(1+k_b)^2} + \alpha_{II} \frac{(1+k_e)^2 k^2 \gamma}{2k_j^2} + \frac{1}{k_j}\left(1+\frac{1}{k_p}\right) + \frac{1}{2k_p^2} + \frac{1}{2}\left(1+\frac{1}{k_p}\right)^2 \right] \quad \text{(Eq 2.2.4-1)}$$

where α_I and α_{II} are the fractional widths of the constrained (I) and unconstrained (II) regions, respectively. The non-dimensional parameters k_e, k_p, k_j, k_b and k_f can be computed as described below:

$$k_\gamma = \sqrt{\frac{1-\nu}{(1-2\nu)(1+\nu)}},$$

$$k_e = \frac{V_r}{k_\gamma}\sqrt{\frac{\rho}{E}},$$

$$k_j = \frac{\rho V_r^{\,2}}{\sigma_y},$$

$$k_b = V_r\sqrt{\frac{\rho}{K}} \quad \text{where } K = \frac{E}{3(1-2\nu)},$$

$$k_p = V_r\sqrt{\frac{\rho}{E_p}} \quad \text{where } E_p = \frac{\sigma_u(1+\varepsilon_\gamma)-\sigma_y}{\varepsilon_r},$$

$$\alpha_I = 1-\alpha_{II} = 1-\sqrt{\frac{V_1}{V_0}} \quad \text{where } \nu_I = \frac{-k_\gamma\sqrt{\rho E}+\sqrt{k_\gamma^{\,2}E\rho+10.4\rho\sigma_y}}{2\rho},$$

where ρ is the density, E the elastic modulus, σ_y the yield strength, σ_u the tensile strength, ν is Poisson's ratio, ε_r the reduction in area or the fractional elongation and V_0 the striking velocity, V_F is a material and thickness independent representative of the average velocity, defined as:

$$V_r = \frac{V_0}{1.85}$$

In this model the terms inside the square bracket in the equation 2.2.4-1 correspond to the mechanical properties as well as the striking velocity of interest. Srivathsa et al [6] express the Ballistic Performance Index (BPI) as:

$$\Phi = \left[\frac{\alpha_I}{2(1+k_b)^2}+\alpha_{II}\frac{(1+k_e)^2k^2{}_\gamma}{2k_j^{\,2}}+\frac{1}{k_j}\left(1+\frac{1}{k_p}\right)+\frac{1}{2k_p^{\,2}}+\frac{1}{2}\left(1+\frac{1}{k_p}\right)^2\right]$$

In the BPI the first two terms represent the elastic components, the third and the fourth terms represent the plastic components and the last term corresponds to the kinetic energy component and Φ is a dimensionless parameter. The strain-hardening rate H is computed as:

$$H = \frac{\sigma_u(1+\varepsilon_r)-\sigma_y}{\varepsilon_r} \qquad (2.1)$$

The strain-hardening rate affects the plastic wave velocity in the material, which essentially determines the extent of plastic deformation in the region of impact.

The authors have applied this model to the following materials:

Table (2.6): Materials tested and their properties [6]

Material	Density [kg/m^3]	Yield strength [MPa]	Tensile strength [MPa]
Mild steel	7800	325	691
Aluminium	2720	130	217
Steel-A	7800	1068	1210
Ti-6Al-4V	4550	990	1050
Al-2024	2770	345	565
Steel-B	7800	1610	1860

They observed that from the ballistic performance:

- Maraging steel is only 1.4 times better than mild steel despite its higher strength. This has been confirmed experimentally [8];
- The BPIs of Steel-S and Steel-B are 1.55 and 2.33, which agreed with the experimental results;
- The Aluminium alloy Al-2024 is nearly 2.2 times better than mild steel. Also, the performance of Ti-6Al-4V is 1.9 times better than that of mild steel.

It can be seen that merely increasing the strength of the material does not necessarily lead to significantly improved performance. This observation is highly significant and will be returned to later in this study on new experimental steels for advanced ballistic performance.

2.2.5. Fracture prediction under high-velocity localised impact

It is well known that the dynamic strength of hard metal sheets and their fracture strength are not identical to those determined for static loading or for low strain rates. Several fracture criteria have been postulated throughout the years. In the present study two of them are presented.

In 2004, Lee and Wierzbicki [9] have postulated that fracture initiates at the critical point of the structure when the accumulated equivalent plastic strain $\bar{\varepsilon}$ with a suitable weighting function, reaches a critical value of:

$$\int_0^{\bar{\varepsilon}_f} f\left(\frac{\sigma_m}{\bar{\sigma}}, \bar{\varepsilon}, T\right) d\bar{\varepsilon} = D_C$$

where $\bar{\varepsilon}_f$, the upper limit of the integral, is the equivalent strain to fracture; f is a weighting function dependent on the stress triaxiality and is defined as the ratio of the hydrostatic mean stress σ_m to the von Mises equivalent stress $\bar{\sigma}$, $\bar{\varepsilon}$ the strain rate, and T the absolute temperature; D_C is a critical damage value of the specific material. The

authors [9] observed three regimes for the fracture mechanisms depending on the stress triaxiality value:

- for a stress triaxiality larger than 1/3 the fracture is controlled by the mechanism of void nucleation, growth and coalescence;
- under negative stress triaxiality the so-called shear decohesion becomes the fracture mechanism; and
- the third regime is a combination of the other two.

It should be pointed out that their study strictly only applies to the prediction of the onset of fracture of uncracked bodies. They further assumed that ductile crack propagation is essentially a process of continuous reinitiation ahead of the crack, so that the same micro-structural events occur in front of the crack tip of previously existing crack, as in the region of a flawless body in which the crack initiates [10]. They have also considered the possible dependence of the fracture criterion on the strain rate and temperature. However Borvik et al. [11-12-13], and Hopperstad et al. [14] have recently shown that the effect of strain rate and temperature on the fracture strain are much smaller than that of any stress triaxiality for Weldox 460E steel.

2.2.6. Shock induced transitions and transformations

The effect of target strength on the perforation of steel plates using different projectile nose shapes, has recently been investigated by Dey and co-workers [15]. They confirm as modelled by Zukas [5], that when a blunt projectile hits the target, the material in front of the projectile accelerates, while the rest of the target is relatively stationary as shown in Figure 2.5.

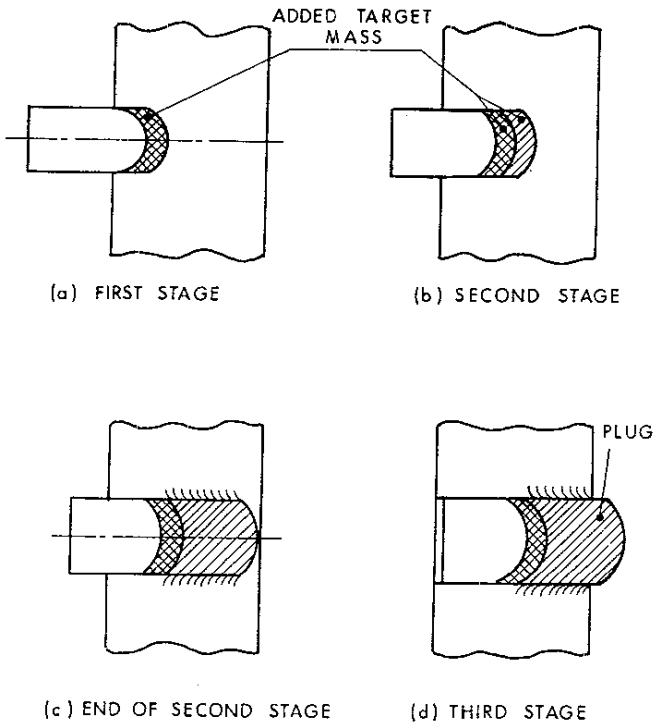

Figure 2.5. Three-stage perforation model showing the increase in the effective mass of the bullet as it progresses through the plate

Hence, the deformation localises in narrow shear bands under adiabatic conditions where the shear strain, shear strain rate and temperature may locally be very high. According to Bai and Dodd [16], these shear bands may either consist of only *deformed* material or *transformed* material, depending on the temperature that was reached in this localised area. Deformation bands are regarded as zones of intense plastic shear only, whereas transformation bands are zones of intense shear in which a phase transformation has occurred. When the localised temperature reaches about $720^0 C$, the steel will undergo a phase transformation. In impact problems involving steel targets, temperatures of this order are produced in micro- or milliseconds, before the band is subsequently quenched by heat flow into the surrounding material.

The common thread is that the spalling-strength of the steel is sufficient as an objective characteristic tensile strength of the material at the microsecond scale of dynamic loading. In reality, a preliminary compression of the material takes place during the passing of the compressive pulse front. If this dynamic compression achieves a critical value, irresistible structural changes within the solid occur before the tensile stresses are generated within the spalling zone of the target. Thus dynamic failure during spallation depends on the plastic instability of the material under compression at the wave front of the loading pulse [17]. The plastic instability can be considered as a strain-rate dependent structural phase transition by means of which the shock wave itself establishes the microstructural features on a mesoscopic scale. Micro-deformation models based on the solution of a non-linear sine-Helmholtz equation, predict a non-stable behaviour of the crystal lattice that is subjected to shear deformation in the non-linear elastic region of loading. This instability leads to the nucleation of large-scale structures such as meso-rotations, shear bands and their combinations. At higher strain gradients a bifurcation transition takes place, which results in the nucleation of structures on a mesoscopic scale commonly seen in microstructural investigations [17]. In accordance with a generally accepted classification (Panin et al., 1982) the microstructural size defining a mesoscopic scale ranges from about 7 to 10 μm.

The transition to a new regime of dynamic deformation can be considered as a structural phase transformation initiated by shock loading. Mescheryakov et al [17] have determined the instability threshold to be at 307 m/s. According to their observation on a set of steels, fracture occurs by a cleavage mechanism at impact velocities less than 307 m/s. However, at impact velocities higher than the instability threshold, blocks of grains and brittle fragmentation become the mechanism of fracture.

2.2.7 Role of material properties

The penetration depth upon impact loading is known to be determined on the basis of a modified Bernoulli equation (Hohler and Stilp, 1990):

$$Y + \frac{1}{2}\rho_{imp}(v-u)^2 = \frac{1}{2}\rho_t u^2 + R, \qquad \text{(Eq 2.2.7-1)}$$

where v is the impactor velocity, u is the particle velocity in the material of the target, Y and R are empirical constants defining the dynamic strength for the material of the

penetrator and target respectively. It is claimed that the physical meaning of parameters Y and R remains to unclear (Hohler and Stilp, 1990).

The value of R takes into account any deviation in behaviour of the material of the target from the hydrodynamic model of penetration.
Micromechanisms of dynamic deformation responsible for the physical nature and value of R are the subject of investigations on microplasticity. The parameter R is often identified with dynamic hardness H_D which is related to the dynamic yielding limit, Y_D, by the following dependence (Tate, 1967; Lasarev et al., 1993):

$$H_D = (3-3.5)Y_D \qquad (2.2.7\text{-}2)$$

The dynamic yielding again is determined by the Hugoniot elastic limit, σ_{HEL}:

$$Y_D = \frac{1-2\nu}{1-\nu}\sigma_{HEL} \qquad (2.2.7\text{-}3)$$

where ν is Poisson's ratio. The main conclusion [17] following from the analysis of peculiarities of high-velocity penetration and also from the analysis of experimental data, is that the strength-component of the resistance of solids to penetration (as a complementary factor for the inertial forces) is determined by the resistance to plastic deformation. This means that if the character of the plastic deformation changes, for example, because of a change of the structural mechanism of deformation, the strength-component of the resistance to penetration changes as well.

Rosenberg et al [18] have investigated the strong dependence of the penetration on a rod's aspect ratio, the so-called " L/D effect ", by rewriting the modified Bernoulli equation as:

$$\frac{1}{2}\rho_{imp}(v-u)^2 = \frac{1}{2}\rho_t u^2 + R_t \qquad (2.2.7\text{-}4)$$

They have observed that the term R_t is reasonably independent of the impact velocity as well as the densities of the rod and target, but is strongly dependent on the target strength. R_t may reach critical values as high as 5.5GPa, whereas Y_D may reach only 2GPa.

2.2.8. Prediction of the martensite start temperature M_s and the Driving Force $\Delta G^{\gamma\rightarrow M}$ for the martensitic transformation

Much work has been done to assess the various factors that determine the type or morphology of martensite that forms upon quenching steels from the austenite region. The influence of temperature, composition, magnetic character of the austenite, quench rate, stacking fault energy, shear strength of the austenite and driving force for the martensite formation have been investigated by various authors.

The free energy change accompanying the martensitic transformation may be expressed as:

$$\Delta G^{\gamma\rightarrow m} = \Delta G^{\gamma\rightarrow\alpha} + \Delta G^{\alpha\rightarrow m} + \Delta G^{*} \qquad (2.2.8\text{-}1)$$

$\Delta G^{\gamma\to m}$ is the driving force required for the transformation from austenite to martensite, $\Delta G^{\gamma\to\alpha}$ is the sum of the chemical and structural free energy change from the austenite to the ferrite at equilibrium, $\Delta G^{\alpha\to m}$ is the structural free energy change from ferrite to martensite, ΔG^{*} is Zener's ordering energy from which Zener's ordering parameter Z has been evaluated by Fisher [19] as:

$$\Delta G^{*} = -2.12\times10^{5} X_C^2 Z^2 + 2.77 X_C T\phi \ \text{J.mol}^{-1} \qquad (2.2)$$

Z = Zener's ordering parameter:

$$\phi = 2(1-Z)\ln(1-Z) + (1+2Z)\ln(1+2Z) \qquad (2.3)$$

The maximum values of Z and ϕ are 1 and 3.295.

$\Delta G^{\alpha\to m}$ has been evaluated with the assistance of the result for Fe-C [20] as:

$$\Delta G^{\alpha\to m} = 2.1\sigma + 900\,\text{J.mol}^{-1} \qquad (2.4)$$

in which σ is the yield strength of austenite at the M_s temperature. It may be approximated for Fe-Mn-C systems by [20]:

$$\sigma = 127.4 + 3920 X_C + 490 X_{Mn} + 0.265(800 - M_S)\ \text{MN.m}^{-2}\ [20]. \qquad (2.5)$$

Morozov et al [21] studied the transformation in Fe with 0.01% C from low to very high cooling rates. They found four arrest temperatures corresponding to four plateaux and denoted them I, II, III and IV. They identified plateau III with the formation of martensite by slip (lath martensite) and plateau IV with the formation of martensite by twinning (plate martensite). Plateau I is mainly due to the formation of incoherent equiaxed α and plateau II is mainly caused by the transformation of austenite to acicular ferrite (AF) or Widmanstätten ferrite. Depending on the cooling rate there are then two M_s temperatures and not one. The plateaux of transformation are illustrated in Figure 2.6 for the Fe-Ni-C system. The two M_s lines intercept at low M_s temperatures [21].

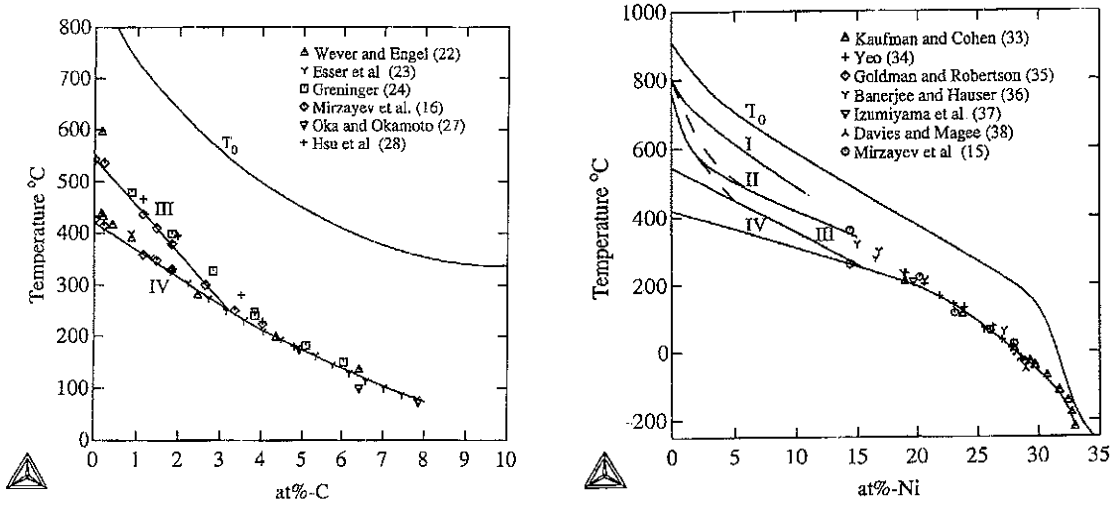

Figure 2.6. Plateaux of transformation and intersection of M_s lines for the Fe-Ni-C system [21]

Table (2.7) presents the intersection temperatures for the two M_s lines as reported by different researchers in varying the cooling rate up to $5x10^5$ K/s in Fe – C alloys containing from 0.01% C up to 0.89% C and for some Fe-X systems.

Table (2.7): Temperature [°C] of intersection of the two M_s lines

	Mizrayev et al [16c]	Mizrayev et al [16c]	Shteynberg et al [16d]	Mizrayev et al [16e]	Mizrayev et al [16f]	Zhao and Jin [16g]	Zhao	Wilson	Wilson
Fe-C	342	284			252	250	244	232	
Fe-Ni	392					0	0		200
Fe-Mn			300			346			
Fe-Cr				300			323		

The Lacher, Fowler and Guggenheim (LFG) model for the calculation of $\Delta G^{\gamma\to\alpha}$ in multiple component systems, which was first proposed by Aaronson et al. [22] by incorporation it with Zener's work [23], may be expressed as:

$$\Delta G^{\gamma\to\alpha} = RT(5-16X_C)\ln(1-2X_C) - 4RT(1-X_C)\ln(1-X_C) + 7RTX_C\ln(3-4X_C) -$$
$$4RTX_C\ln 2 - 6RT(1-3X_C)\ln(\delta_\gamma + 1 - 3X_C) + 6RT(1-X_C)\ln(\delta_\gamma + 1 - X_C) - 8RTX_C\ln(\delta_\alpha + 3 - 5X_C)$$
$$+ X_C\left[\left(\Delta\bar{H}_C^{\alpha} - \Delta\bar{H}_C^{\gamma}\right) - \left(\Delta\bar{S}_C^{xs(\alpha)} - \Delta\bar{S}_C^{xs(\gamma)}\right)T\right] + (1+X_C)$$
$$\times\left[141\sum_i X_i\left(\Delta T_{Nm}^i\right) + \Delta G_{Fe}^{\gamma\to\gamma}\times\left\{T - 100\sum_i X_i\Delta T_{mag}^i\right\}\right] \qquad (2.6)$$

where

$$\delta_\alpha = \left[9(1-X_C)^2 - 4X_C(3-4X_C)J_\alpha\right]^{1/2} \qquad (2.7)$$
$$\delta_\gamma = \left[(1-X_C)^2 - 4X_C(1-2X_C)J_\gamma\right]^{1/2} \qquad (2.8)$$
$$J_{\alpha,\gamma} = 1 - \exp(-\omega_{\alpha,\gamma}/RT) \qquad (2.9)$$
$$\omega_\alpha = \text{-}25{,}310 \text{ J.mol}^{-1}$$
$$\omega_\gamma = 1380 \text{ J.mol}^{-1}$$
$$\Delta\bar{H}_C^{\alpha} = 109{,}680 \text{ J.mol}^{-1}$$
$$\Delta\bar{H}_C^{\gamma} = 38{,}460 \text{ J.mol}^{-1}$$
$$\Delta\bar{S}_C^{xs(\alpha)} = 39.90 \text{ J.mol}^{-1}.\text{K}^{-1}$$
$$\Delta\bar{S}_C^{xs(\gamma)} = 10.65 \text{ J.mol}^{-1}.\text{K}^{-1}$$

T refers to the M_s temperature in absolute degrees and is the term to be evaluated; X_C and X_i are the mole fractions of Carbon and the ith substitutional alloying element; ΔT_{mag} and ΔT_{Nm} are the magnetic and non-magnetic components respectively affecting the $\Delta G^{\gamma\to\alpha}$ of

pure iron, or the displacement in M_s temperature of pure iron by 1 at.% of alloying element. From the Aaronson, Domian and Pound (ADP) model [21] ΔT_{mag} =-35.5 K and ΔT_{Nm} =-37.5 K.

Wang et al [24] have developed an advanced set of equations in which combined binary effects between sets of alloying elements were taken into account for the estimation of the M_s temperatures. The nominal concentration of binary terms was defined as the square root of the products of the mass percentages of two chemical constituents.

$$w_{i-j} = \sqrt{w_i w_j} \text{ leading to the general equation: } M_s = k_0 + \sum k_{ij} \sqrt{w_i w_j}$$

$$\begin{aligned} Ms\left({}^0C\right) = {} & 540 - 584.9w_C - 23.1w_{Si} - 117.7w_{Mn} - 42.5w_{Cr} - 49w_{Mo} - 62.5w_{C-Si} \\ & + 178.3w_{C-Mn} - 10.0w_{C-Cr} + 52.5w_{C-Mo} + 117.2w_{Si-Mn} + 50.9w_{Si-Cr} - 142.2w_{Si-Mo} \\ & - 129.2w_{Mn-Cr} - 9.7w_{Mn-Mo} + 69.9w_{Cr-Mo} \end{aligned} \quad (2.10)$$

This equation may be applied to typical steel compositions in the range of 0.2 to 0.5%C, 0.5 to 2%Si, 0.5 to 2.0%Mn, 0.5 to 2.0%Cr and 0.1 to 0.7%Mo.

Note that with binary interaction effects, some positive changes in the M_s temperature are to be expected as opposed to the generally negative effects with single element considerations. Other formulae proposed for the M_s estimation in ferrous steels are summarised in the following table:

Table (2.8). Different formulae for the estimation of M_S temperatures in steels

Reference	M_S [K], all compositions in wt.%
[27]	$772 - 316.7C - 33.3Mn - 11.1Si - 27.8Cr - 16.7Ni - 11.1Mo - 11.1W$
[28]	$811 - 361C - 38.9Mn - 38.9Cr - 19Ni - 27.8Mo$
[29]	$785 - 453C - 15Cr - 16.9Ni - 217(C)^2 - 71.5(C)(Mn) - 67.6(C)(Cr)$

All these attempts that were made at modelling the compositional dependency of M_s using linear regression or similar methods, are classified as non-adaptative [30] because the 'shape' of the function is predetermined by the authors rather than adapted to the data. Neural networks, as opposed to traditional linear or polynomial regression methods, do not impose a shape of the function on the data. In contrast, neural network methods that are currently under development are adaptive functions.

From these empirical formulae it appears that Nitrogen decreases the M_s temperature more largely than Carbon. This is attributed to its stronger stabilisation of the austenitic matrix due to a larger solid solution strengthening effect. The same observation [30] may be arrived at on the effects of Manganese and Molybdenum due to a difference in solid solution strengthening. Hayzelden et al [31] have investigated the effect of the austenite grain size and the dislocation density on the M_s temperature. In an Fe - 0.38%C - 26.13%Ni alloy and in the absence of a change in dislocation density, M_s was found to be determined by the grain size of the austenite. For a given grain size, the M_s is raised by an increase in dislocation density. In this case the microhardness of the austenite is unaffected by a reduction in grain size but is raised by an increase in dislocation density within the grains.

The depression in M_S in the fine-grained alloy could not be explained by the Hall – Petch strengthening of the austenite and was believed to result from the segregation of active martensite nuclei into a few small grains, a suppression of the autocatalytic stimulation of martensite plates between adjacent grains and a possible reduction in the number of potential martensite nuclei.

From their study on the heterogeneous nucleation of martensite within the vicinity of grain boundaries using an SEM-EBSD method, Ueda et al [32], observed that only some grain boundaries with a specific character could activate martensitic transformations effectively. These include 90°<211> symmetric tilt boundaries that acted as a favourable site for martensite formation while 90^0<211> twist boundaries did not. In the vicinity of grain boundaries, some martensite variants with the habit plane almost parallel to the grain boundary were preferentially formed from amongst 24 possible habit plane variants. The equivalent variants were adjoined at the tilt boundary to maintain the compatibility of the transformation strains across the boundary, resulting in an increase in the martensite-start temperature. These authors have defined this type of nucleation as "cooperative nucleation (CN)". They have estimated the difference in M_s temperatures for different tilt angles in the vicinity of the grain boundaries as 50K. A grain boundary may reduce the strain energy for the nucleation of martensite. In particular, the symmetric tilt boundary 180^0<211> demonstrated the highest M_s temperature. It suppresses the growth of embryos into martensite (the self-accommodation of a group of variants), since the compatibility requirements are maintained at the boundary and result in higher M_s temperatures and more effective CN.

Many researchers have succeeded in explaining various phenomena or crystallographic features of phase transformations using Eshelby's inclusion theory [33]. According to this theory, the elastic strain energy due to martensitic transformation may be calculated from the shape strain matrix as follows: The shape strain matrix must be first converted to the symmetric matrix $\varepsilon_{ij}{}^{T}$, which is given by

$$\varepsilon_{ij}{}^{T} = \frac{S_{ij} + S_{ji}}{2} - \delta_{ij} \ , \qquad (2.11)$$

where δ_{ij} is the Kronecker delta [33]. δ_{ij} =1 for i = j and δ_{ij} = 0 for i≠j. The strain energy $U_{0,}$ generated by the shape change of ε_{ij} in an elastic medium, is given by:

$$U_0 = \int_0^{\varepsilon_{ij}} \sigma_{ij} d\varepsilon_{ij} \qquad (2.12)$$

Since Hooke's law is applicable in an elastically isotropic matrix, the elastic strain energy can be expressed in terms of the strain components as follows:

$$U_0 = \frac{\nu G_M}{1-2\nu}\left(\varepsilon_{xx} + \varepsilon_{yy} + \varepsilon_{zz}\right)^2 + G_M\left(\varepsilon_{xx}{}^2 + \varepsilon_{yy}{}^2 + \varepsilon_{zz}{}^2\right) + 2G_M\left(\gamma_{xy}{}^2 + \varepsilon_{yz}{}^2 + \varepsilon_{xz}{}^2\right) \qquad (2.13)$$

where G_M is the shear modulus and ν is Poisson's ratio. When a martensite plate nucleates independently in a single crystal, the strain energy U_0 is calculated to be about 1500 J/mol.[34].

Borgenstam and Hillert [35] presented a very good summary on the thermodynamic theory of the martensitic transformation in Fe-X systems. The following paragraph is based on their work and on the general observation by Nishiyama [36]. Johansson [37] was the first to publish in 1937 a thermodynamic analysis of the α and γ phases in the Fe-C system. He discussed the martensitic transformation, presuming that martensite cannot form at that temperature where α and γ have the same Gibbs free energy, but it requires further undercooling for the necessary driving force. He proposed that this extra driving force results from the Carbon atoms within martensite being "frozen" into the positions inherited from the parent γ, and he believed that those positions would give a higher free energy as well as a lower entropy than in α with its random distribution of the Carbon atoms. Zener [38] instead assumed that martensite, which is tetragonal at higher Carbon contents because of the non-random positions of the Carbon atoms, would have a lower free energy because of the Carbon atoms collaborating and thus minimising the strain energy caused by the presence of these atoms in interstitial sites of insufficient size. He even proposed that there is a temperature-composition region where the tetragonal martensite with the non-random distribution of Carbon atoms would have a lower Gibbs free energy than α with a random distribution. He developed a simple theory of ordering and by minimizing the Gibbs free energy, it was possible to predict the degree of order at equilibrium. When evaluating the driving force for the martensitic transformation he assumed that martensite would have those equilibrium ordered properties. Fisher [19] made a more thorough analysis of the Gibbs energy of the ordered α phase by evaluating the driving force for martensite formation and determined values for the Zener's ordering driving force ΔG^* and ordering parameter Z as presented earlier in this paragraph. Many evaluations of the driving force for martensite formation have been published over the years with most of them taking Zener ordering into account.

It should be emphasized that the idea of Carbon atoms inheriting their positions from the parent γ is based on the assumption that the rate of transformation is so high that there is not enough time for Carbon atoms to redistribute by diffusion during the actual transformation. It seems that this could apply to the edgewise growth of plate martensite but possibly not to the growth of lath martensite. If this is so, then the equilibrium degree of order should be used for lath martensite. Furthermore, at very high growth rates there is not even time for the reaction heat to diffuse away and the temperature will be higher at the γ/α interface than in the rest of the system [39].

After these results [19, 35, 36, 37, 39] the driving force for the formation of plate martensite may have a constant value of about 2100 J/mol. For lath martensite it may vary linearly with the formation temperature, possibly from 500 J/mol at $800\,^0C$ to 2100 at $250\,^0C$.

Another uncertainty in the description of the Gibbs free energy of the α phase is the effect of Carbon on the ferromagnetic transition in the α phase. The analysis of the properties of the α phase made by most researchers is made with the assumption that the magnetic properties are not affected by Carbon. Earlier, Nishiyama [36] had already voiced his reservation on the validity of the thermodynamic theories of the martensitic transformation. He stated that in the current thermodynamic theories on the growth of a martensite nucleus, the interfacial and internal chemical energies are considered to be dominant, as in the case of crystallization in a liquid. In addition because of the solid medium, the strain energy of the transformation is also taken into account. These theories, however, assume thermal

equilibrium and ignore the microstructural and crystallographic characteristics of the martensitic transformation. He, therefore, felt that such theories are not reasonable and it would be better to rather construct a thermodynamic theory that takes microscopic structures into consideration.

2.2.9. Kinetics of the martensitic transformation

The nucleation of martensite during cooling is believed to take place at structural imperfections in the parent phase. These pre-existing embryos (defects) are stimulated to grow into martensite crystals at different degrees of undercooling below the M_s temperature as they have different energy barriers to activation. Growth can, however, be very fast. Each nucleation event directly leads to the formation of a typical volume of the new phase. Thus, the volume fraction of martensite varies only with the degree of undercooling, which expresses the athermal character of the transformation. Koistinen and Marburger [40] have postulated that the evolution of martensite formation in a sample that is initially fully austenitic, may be described by:

$$f = 1 - e^{C_1(Ms-T)} \qquad (2.14)$$

where f is the volume fraction of martensite in the sample at temperature T below M_s, and C_1 is a constant. This volume fraction is defined as the volume of martensite divided by the volume of austenite that exists in the sample prior to the formation of martensite. Magee [41] derived the following empirical equation from first principles, assuming that in a temperature interval dT, the incremental number dN of new martensite crystals (plates or laths) that form per unit volume of austenite is proportional to the increase in driving force $\Delta G^{\gamma\rightarrow\alpha'}$ due to the temperature decrease dT:

$$\frac{dN}{dT} = -C_2 \frac{d\left(\Delta G^{\gamma\rightarrow\alpha'}\right)}{dT} \qquad (\Delta G^{\gamma\rightarrow\alpha'} < 0) \qquad (2.15)$$

where C_2 is a positive constant expressing the proportionality between the increase in driving force and the consequent increase in density of activated nucleation sites. The change in the volume fraction of martensite corresponding to the temperature decrease dT is then given by:

$$\frac{df}{dT} = \Omega(1-f)\frac{dN}{dT} \qquad (2.16)$$

where $(1-f)$ is the volume fraction of austenite available for further transformation and Ω is the average volume of martensite per newly formed crystal. Combining these two equations, yields:

$$\frac{df}{dT} = -\Omega(1-f)C_2 \frac{d\left(\Delta G^{\gamma\rightarrow\alpha'}\right)}{dT} \qquad (2.17)$$

Assuming that Ω, C_2, and $\frac{d\left(\Delta G^{\gamma\rightarrow\alpha'}\right)}{dT}$ are constant over the extent of the transformation and integrating from M_s (f = 0) to T gives:

$$\ln(1-f) = \Omega C_2 \frac{d\left(\Delta G^{\gamma\rightarrow\alpha'}\right)}{dT}(Ms - T) \qquad (2.18)$$

This equation is equivalent to equation (2.14) with the positive parameter C_1 expressed by:

$$C_1 = -\Omega C_2 \frac{d\left(\Delta G^{\gamma\rightarrow\alpha'}\right)}{dT} \qquad (2.19)$$

Thus $\ln(1-f)$ is expected to vary linearly with T when the nucleation and growth of the martensite crystal in a sample obey the characteristics as proposed by Magee. The assumption that Ω is a constant is in contradiction with the Fisher model [42], which assumes that Ω decreases strongly as the transformation progresses. Van Bohemen et al [43] have fitted their experimental data to the Koistinen and Marburger equation for the following steels:

Table (2.9). Chemical composition of steels used in Van Bohemen's study [43]

Steel	C	Si	Mn	P	S	Cr	Cu	Ni
C60	0.6	0.39	0.50	0.020	0.04	0.23	0.21	0.07
C70	0.7	0.37	0.68	0.027	0.04	0.29	0.22	0.16
C80	0.8	0.41	0.61	0.012	0.05	0.28	0.23	0.15

They have found the following values for the fitting parameters of the kinetic equation:

Table (2.10). Fitting parameters for the kinetics of the martensitic transformation

Steel	Ms $\left({}^0C\right)$	$C_1\left(K^{-1}\right)$	$d\Delta G^{\gamma\rightarrow\alpha'}/dT\left(J/mol\,{}^0C\right)$	ΩC_2 $\left(mol/kJ\right)$	$f_A(-)$
C60	282	0.067	7.2	9.3	0.90
C70	248	0.055	7.0	7.9	0.95
C80	211	0.046	6.9	6.7	1.00

2.2.10. Crystallography and morphology of martensite, general considerations and definition of martensite

In optical microscopy one may distinguish between two kinds of martensite: lath and plate types. Lath martensite is usually formed at low alloy contents (or at high M_s) and plate martensite at high alloy contents (or low M_s) and a mixture of the two types occurs in between. At higher magnifications with transmission electron microscopy it appears that lath martensite is a highly dislocated structure and it probably has formed through slip. The midrib of plate martensite is heavily twinned and it probably has formed by a twinning mechanism. The outer part of a martensite plate is often dislocation-rich and without twins and sometimes it resembles lath martensite in optical microscopy.

A martensitic transformation is a phase transformation that occurs by cooperative atomic movements.

That a given structure is produced by a martensitic transformation can be confirmed by the presence of the diffusionless character, the surface relief, and the presence of many lattice defects. Such characteristics are, therefore, criteria for the definition of martensite [36]. Martensite may have many other characteristics, which though suggesting the presence of martensite, are not necessarily proof in themselves that a martensitic transformation has occurred. For example, high hardness was believed a necessary property of martensite at the time when the word "martensite" was first adopted but it is no longer regarded as a good criterion. Equally, the rapidity of the transformation does not necessarily lead to martensite. Though in most steels the time of formation of an α' crystal is of the order of 10^{-7} seconds, the growth is so slow that the process in some alloys may be followed under an optical microscope [36]. The existence of a habit plane and orientation relationship with the parent phase is a necessary consequence of the coherency of a martensitic transformation; although in turn it is not a sufficient criterion, because coherent precipitates that are definitely not classified as martensite also have such characteristics.

A number of types of martensite have been observed in nonferrous alloys. In Carbon and low alloy steels with M_s temperatures well above room temperature, the complete suppression of Carbon diffusion during quenching is virtually impossible to attain. In the lowest Carbon steels with high M_s temperatures the Carbon mobility is sufficient to even cause epsilon carbide ($Fe_{2.4}C$) precipitation in the martensite during quenching to room temperature, a process referred to as autotempering [60]. A more common manifestation of Carbon diffusion in martensite during quenching is its segregation to dislocations and lath boundaries. Speich [51] has presented indirect evidence based on electrical resistivity measurements, for the segregation of Carbon atoms in Iron – Carbon martensite. He reasoned that the *lower slope* in the change in resistivity curve for martensitic structures containing less than 0.2% C, corresponds to complete segregation of the Carbon to dislocations, leaving the ferrite free of the scattering centres due to carbon trapped in octahedral interstitial sites. The *higher slope* in the change in the resistivity curve in martensitic microstructures in steels containing more than 0.2% C was attributed to the scattering by carbon atoms randomly distributed in octahedral sites of the martensite. The measurement of increasing tetragonality of Fe – C martensite crystals with increasing Carbon concentration by X – ray diffraction [61] certainly verifies that a significant fraction of Carbon atoms are retained in octahedral sites in untempered higher Carbon steels. Direct evidence for Carbon atom segregation to dislocations during quenching and room temperature aging of martensite has been obtained by Smith and his colleagues [62] with field ion / atom – probe microscopy. They confirmed Speich's conclusion that almost 90% of the Carbon atoms in a 0.18%C martensite are segregated to dislocations. Mader and Krauss [63] showed that packet martensite consists of dislocated laths (α') which form in steels when the M_s transition temperature is above 350^0C. This temperature is strongly dependent on the steel's composition, especially its Carbon content. McMahon and Thomas [64] showed that the dislocated structures at martensitic lath boundaries (α') were in fact thin microlayers of retained austenite. The identification of such thin layers of retained austenite requires diffraction analysis through electron microscopy. This interlath austenite was revealed by the authors through high resolution lattice imaging electron microscopy from which it was suggested that there was considerable Carbon enrichment at the α'/γ interfaces, i.e. also suggesting Carbon movement. Heat treatments of α'/γ phase mixtures in the range 300 to 500^0C result in the austenite decomposing to interlath carbides. The structure becomes similar to lower bainite, causing embrittlement in directions transverse with respect to prior austenite.

Liu and Dunne [65] investigated the nature of the terminating interfaces of the twin volumes in Cu-14%Al-3.4%Ni twinned martensite, using Atomic Force Microscopy. Although twin relief was generally evident in the random sections they have examined, well-defined interfacial facets corresponding to the terminating twin volumes were not observed. Instead, side-plates extending beyond the habit plane were common, being associated with the smaller of the twin volumes. They noted that the twin plane is close to the habit plane and its extension ahead of the general interface with its own twinned substructure, is probably related to the plate growth mechanism. From the observed difference in side-plate extensions between thermal and stress-induced plates they suggest that growth occurs by the motion of only one interface in providing strain accommodation of the applied stress, whereas for thermal martensite the growth is constrained by the surrounding matrix and the stresses imposed by transformation shear and a volumetric change. Moreover fine twins on a system other than the primary twinning system were also observed for the thermal martensite in their investigation.

2.2.10.1. Habit plane

Christian [44] noticed that the habit plane is usually one of three types:

- planar, irrational and semi-coherent, separating a single-crystal parent from a slipped and/or faulted single-crystal product;
- planar, irrational and separating a single-crystal parent from a twinned product; or
- curved and thus macrospically displaced from the “true” habit plane, because of interfacial steps.

The martensite interface is observed to be glissile, at least for the forward transformation, and it is implied that either:

- planar sections migrate as a unit, consisting of twin-parent volumes or surface dislocations; or
- steps consecutively sweep across the whole interface.

Christian [45] concluded that the invariant plane strain condition might only be met for “unconstrained” single interface transformations. In polycrystalline austenite, local constraints such as coherency strains could induce the operation of a more complex lattice invariant shear, giving significant habit plane variations. Kennon and Dunne [46] explored the suggestion by Christian , in the case of $\gamma_1^{'}(2H)$ plates in a cubed-shaped single crystal Cu-Al-Ni alloy. After accurate tilt and habit plane trace measurements with an estimated experimental error in the habit plane normal of less than $\pm 1^0$, they concluded that even in the case of unconstrained transformation, a real variability in the habit plane normal could occur. A close examination of the interface of $\gamma_1^{'}$ martensite by the authors indicated that variations in transformation twin width are not uncommon, resulting in changes in the local average interface plane. The habit plane can curve to accommodate minor localised constraints and any atomic matching across the interfacial twin facet must be high. This observation has been confirmed recently in the case of a {225} martensite transformation in Fe-Cr-C alloy by Lin et al. [47].

Tadaki and Shimizu [48] suggested that the temperature dependence of the lattice parameters of the austenite and the difference between that of austenite and martensite must mean that the crystallography of the transformation will change with the actual temperature of formation of the martensite during the quenching. A continuous spectrum of habit planes is, therefore, possibly to be expected over the transformation temperature range as a function of order and temperature. Dunne and Kennon [49] concluded from the systematic type of habit plane variation, that there is clearly a scatter which is not accounted for by the theory and which is a characteristic feature of the martensitic transformation. Moreover, habit plane "flexibility" is likely to be a characteristic feature of martensite plates.

Given the plane and direction of the lattice invariant shear, the lattice correspondence between the parent and martensite and the pure strain, the crystallographic theory predicts the habit plane on the basis that it is exactly invariant. However, Dunne and Kennon [49], noticed that the invariance may only be local because of localised plastic and/or elastic constraints, leading to macroscopic habit plane measurements which may differ significantly from the predicted plane. Local changes in the invariant shear will occur with strains created by the plate itself or by prior transformation. Accommodating slip or faulting can occur in the parent phase or in the martensite, influencing the form of the moving interface. On the basis of their analysis of habit plane scatter, Dunne and Kennon [49] concluded that the response to the question: "how regular is the habit plane?" must be: "not very". Moreover the variability should be regarded as a characteristic feature of the transformation rather than an anomaly. As the literature shows, good correspondence between measured and predicted habit planes is usually restricted to precisely controlled conditions in which limited transformation occurs in a coarse grained or a single crystal parent phase. In other circumstances and particularly for transformations involving a large volume change, considerable habit plane variability should be expected.

Morito et al [50], have examined the morphology and crystallography of lath martensite in Fe-C alloys with different Carbon contents such as 0.0026, 0.18, 0.38 and 0.61 mass %C by means of optical microscopy, by SEM and by TEM. Their main findings were: as the carbon content increased from 0.0026% to 0.61%, the block and packet size of the martensite units decreased; the orientation relationship between austenite and martensite was close to the Kurdjumov-Sachs relationship and some laths seemed to have nearly the Nishiyama relationship; twenty-four variants in the K-S relationship were suggested as presented in Table (2.11).

In low Carbon alloys (typically 0.0026%C – 0.38%C), martensite packets consisted of well-developed parallel blocks with three blocks (with different orientations) in each packet. Each block consisted of laths of two specific K-S variant groups (called a "sub-block") which were misoriented by small angles of about 10°; and in high Carbon alloys (>0.61% C), packets consisted of fine blocks whose width were a few microns. Blocks consisted of laths with a single variant and six blocks with different orientations existed in a packet.

In martensitic Fe-C alloys and low-alloy Carbon steels with above-room temperature M_s temperatures, Krauss [51] observed that it was impossible to prevent Carbon diffusion during quenching, and strengthening of martensite becomes dependent on static and dynamic strain aging due to Carbon atom interaction with dislocation substructures. The substructure of the martensitic matrix appears to be the dominant strengthening component in these steels.

Table (2.11). Variants in K-S relationship [50]

Variant N_0	Plane parallel	Direction parallel $[\gamma]//[\alpha']$	Rotation from variant 1 Axis (indexed by martensite)	Angle [deg.]
V1	$(111)_\gamma$ // $(011)_{\alpha'}$	[-1 0 1] // [-1 –1 –1]	-	-
V2		[-1 0 1] // [-1 1 -1]	[0.5774 – 0.5774 0.5774]	60.00
V3		[0 1 –1] // [-1 –1 -1]	[0.0000 – 0.7071 – 0.7071]	60.00
V4		[0 1 –1] // [-1 1 –1]	[0.0000 0.7071 0.7071]	10.53
V5		[1 –1 0] // [-1 –1 1]	[0.0000 0.7071 0.7071]	60.00
V6		[1 –1 0] // [-1 1 -1]	[0.0000 – 0.7071 – 0.7071]	49.47
V7		[1 0 –1] // [-1 –1 1]	[-0.5774 – 0.5774 0.5774]	49.47
V8		[1 0 –1] // [-1 1 –1]	[0.5774 – 0.5774 0.5774]	10.53
V9	$(1\text{-}11)_\gamma$ // $(011)_{\alpha'}$	[-1 –1 0] // [-1 –1 1]	[-0.1862 0.7666 0.6145]	50.51
V10		[-1 –1 0] // [-1 1 -1]	[-0.4904 –0.4625 0.7387	50.51
V11		[0 1 1] // [-1 –1 1]	[0.3543 –0.9329 –0.0650	14.88
V12		[0 1 1] // [-1 1 -1]	[0.3568 –0.7136 0.6029]	57.21
V13		[0 –1 1] // [-1 –1 1]	[0.9329 0.3543 0.0650]	14.88
V14		[0 –1 1] // [-1 1 -1]	[-0.7387 0.4625 –0.4904]	50.51
V15	$(\text{-}111)_\gamma$ // $(011)_{\alpha'}$	[-1 0 –1] // [-1 –1 1]	[-0.2461 –0.6278 –0.7384]	57.21
V16		[-1 0 –1] // [-1 1 -1]	[0.6589 0.6589 0.3628]	20.61
V17		[1 1 0] // [-1 –1 1]	[-0.6589 0.3628 –0.6589]	51.73
V18		[1 1 0] // [-1 1 -1]	[-0.3022 –0.6255 –0.7193]	47.11
V19		[-1 1 0] // [-1 –1 1]	[-0.6145 0.1862 –0.7666]	50.51
V20		[-1 1 0] // [-1 1 -1]	[-0.3568 –0.6029 –0.7136]	57.21
V21	$(11\text{-}1)_\gamma$ // $(011)_{\alpha'}$	[0 –1 –1] // [-1 –1 1]	[0.9551 0.0000 –0.2962]	20.61
V22		[0 –1 –1] // [--1 1 -1]	[-0.7193 0.3022 –0.6255]	47.11
V23		[1 0 1] // [-1 –1 1]	[-0.7384 –0.2461 0.6278]	57.21
V24		[1 0 1] // [-1 1 -1]	[0.9121 0.4100 0.0000]	21.06

Lath martensite forms in low and medium-Carbon steels and consists of parallel arrays or stacks of board- or lath-shaped crystals. In these steels most of the crystals in a parallel group have the same crystal orientation and the parallel groups are referred to as blocks [52]. As Carbon concentration increases, the parallel or almost parallel crystals in a group, termed packets, may have different orientations and variants of $\{557\}_A$ habit planes around a given $\{111\}_A$ plane [53-54]. Plate martensite crystals form in non-parallel arrays and are characterized by irrational habit planes, including $\{3\ 10\ 15\}_A$,$\{2\ 2\ 5\}_A$ and $\{259\}_A$ [55]. The low M_s temperatures, in high Fe-C alloys and steels, cause the lath martensite crystals to form at temperatures where the lattice invariant deformation is accomplished by twinning and limited dislocation motion occurs.

The morphology of the martensite affects the deformation and strengthening of the microstructure in a number of ways. In lath martensites, the block and packet structures, because of the largely common crystallographic orientation of the parallel laths within the blocks and packets, become the effective grain structures, which control deformation. Similarly, because of common $\{1\ 0\ 0\}_m$ cleavage planes in the parallel laths in blocks and packets of martensite, the size of cleavage facets which produce brittle transgranular fracture is directly related to the packet size [56-57]. Also the morphology of the retained austenite within lath and plate martensites determines whether the austenite will mechanically transform by stress- or strain-induced mechanisms [58]. The non-parallel formation of plate-shaped martensite crystals often results in intraplate microcracking due to the impingement of the plates during quenching [54].

2.2.10.2 Theory of the martensitic transformation

A number of crystallographic and thermodynamic theories have been proposed to explain the transformation mechanisms in martensite formation. In the current thermodynamic theories on the growth of the martensite nucleus, the interfacial and internal chemical energies are considered to be dominant, as in the case of the crystallization in a liquid. In addition in solids, the strain energy of the transformation is also taken into account. Thermodynamic theories assume thermal equilibrium and ignore the microstructural and crystallographic characteristics of the martensitic transformation [36]. The Bowles and Mackenzie model [in 36], one of the phenomenological theories, predicts the crystallographic features such as the habit plane, the strain and the orientation relationships between parent austenite and product martensite. Kelly [59] recently demonstrated that, when applied in a rigorous fashion, the Infinitesimal Deformation (ID) approach is exactly equivalent to the Phenomenological Theory of the Martensitic Transformation (PTMT). The disadvantages of the PTMT are its computational cost and its complexity that makes it less understandable than the physical concepts of the minimization of the strain energy following the well-known Eshelby analysis used in the ID approach.

2.2.11. The Bowles – Mackenzie model [in 36]

2.2.11.1. Lattice parameters and tetragonality of the martensite.

Lattice parameters of martensite and retained austenite can be measured by X-ray diffraction with good accuracy. Cheng et al. [66] noticed a significant redistribution of Carbon atoms and a disappearance of the tetragonality of a 5.1at.%C martensitic steel at room temperature during aging times of less than 50 hours. Carbon atoms segregated to lattice imperfections and also transfer from a/b-type octahedral interstices to c-type interstices, thereby decreasing the c_m parameter at room temperature.

Lyssak and co-workers [67] found that the tetragonality of the martensite is abnormally small for Mn steels. Moreover, there are several alloy systems in which the tetragonality of martensite containing Carbon does not obey the well-known experimental equation:

$$c/a = 1 + 0.046\,p$$

where p is the mass percentage of carbon in the steel.

Kajiwara and Kikuchi [68] made a very extensive and systematic study on the martensite tetragonality in Fe-Ni-C alloys, and found that the tetragonality is quite dependent on the mode of the lattice invariant deformation in the martensite. Uehara et al. [68] have investigated the tetragonality of martensite in high Carbon- Iron alloys containing some Aluminium. From their study it appears that the tetragonality is enhanced by Aluminium and Nickel additions that stop Carbon atoms from moving out of octahedral sites to tetrahedral sites during quenching (auto-tempering). They have measured the tetragonality in martensite containing 2 mass %C and up to 6 mass %Ni using XRD equipment fitted with a cooling unit. Their measurements were done at temperatures as low as 90K.

2.2.11.2. The principal strain.

After measuring the lattice parameters of the parent austenite and the product martensite, the Bowles and Mackenzie (BM) model for predicting the transformation characteristics may be applied as follows:

The principal strains in the Bain distortion denoted by η_i (eta), are represented by:

$$\eta_1 = \sqrt{2}\, a_M / a_\gamma \qquad (2.20a) \qquad \text{along x-1}$$

$$\eta_2 = \sqrt{2}\, a_M / a_\gamma = \eta_1 \qquad (2.20b) \qquad \text{along x-2}$$

$$\eta_3 = c_M / a_\gamma \qquad (2.20c) \qquad \text{along x-3}$$

A unit sphere representing the austenite crystal $x_1^{\,2} + x_2^{\,2} + x_3^{\,2} = 1$ transforms to an ellipsoid $\frac{x_1^{\,2}}{\eta_1^{\,2}} + \frac{x_2^{\,2}}{\eta_2^{\,2}} + \frac{x_3^{\,2}}{\eta_3^{\,2}} = 1$ due to the Bain distortion.
The cones of unextended lines are found from the equation:

$$\left(\frac{1}{\eta_1^{\,2}} - 1\right) x_1^{\,2} + \left(\frac{1}{\eta_2^{\,2}} - 1\right) x_2^{\,2} + \left(\frac{1}{\eta_3^{\,2}} - 1\right) x_3^{\,2} = 0\,. \qquad (2.21)$$

The semi-apex angle Φ' of the cone is obtained from the value of $\frac{x_2}{x_3}$ when $x_1 = 0$:

$$\tan(\Phi') = \left(\frac{x_2}{x_3}\right)_{x=0_1} = \left(\frac{1-\eta_3^{\,2}}{\eta_1^{\,2}-1}\right)^{\frac{1}{2}} \left(\frac{\eta_1}{\eta_3}\right). \qquad (2.22)$$

Φ' gives the positions of the unextended lines after transformation. The initial cone of the unextended lines can be determined by considering a hypothetical inverse transformation, such as α' to γ transformation, i.e. a unit sphere representing the martensite crystal transforms to an ellipsoid representing the austenite.

$$\eta_1^{\,2} x_1^{\,2} + \eta_2^{\,2} x_2^{\,2} + \eta_3^{\,2} x_3^{\,2} = 1 \qquad (2.23)$$

the semi-axes of which are $\frac{1}{\eta_1}$, $\frac{1}{\eta_2}$, $\frac{1}{\eta_3}$. Therefore, it is seen that the equation:

$$\left(\eta_1^{\,2} - 1\right) x_1^{\,2} + \left(\eta_2^{\,2} - 1\right) x_2^{\,2} + \left(\eta_3^{\,2} - 1\right) x_3^{\,2} = 0 \qquad (2.24)$$

represents the locus of all vectors that are unchanged in magnitude due to the hypothetical inverse transformation. The locus is nothing else but the initial cone of the unextended lines. The semiapex angle Φ of the initial cone is calculated from:

$$\tan(\Phi) = \left(\frac{x_2}{x_3}\right)_{x=0_1} = \left(\frac{1-\eta_3^{\,2}}{\eta_1^{\,2}-1}\right)^{\frac{1}{2}} \qquad (2.25)$$

2.2.11.3. Calculation of invariant lines and normal

A plane normal is defined as a vector whose direction is parallel to the normal of the plane and whose magnitude is proportional to the inverse of the interplanar distance. This vector is simply a reciprocal lattice vector. Then a unit sphere (formed by the plane normal) in the austenite lattice transforms to an ellipsoid, whose semi-axes are:

$$\frac{1}{\eta_1}, \frac{1}{\eta_2}, \frac{1}{\eta_3}.$$

The intersection of the ellipsoid with the unit sphere forms a circle, and a cone passing through the circle gives the final position of the plane normal which is unchanged in magnitude. Such a normal is termed an *unextended normal*.

An unextended normal and an unextended line that are also unchanged in direction are termed an *invariant normal* and an *invariant line*, respectively.

Consider x-1 or x-2 is a unit vector parallel to the invariant line. The Bain distortion allows x_i also to transform through the equivalence:

$$\underline{x}_i = Bx_i . \qquad (2.26)$$

Because x_i is unchanged in length, $x_i' x_i = 1$ holds. In addition, $p_2' x_i = 0$ because the shear plane p_2' of the complementary shear must involve three equations for x_i.

Assuming: $p_2' = (1/\sqrt{2})(101)$ (2.27)

one obtains the following three equations for x_i:

$$x_1^2 + x_2^2 + x_3^2 = 1 \qquad \text{equivalent to } P_1 = R(BPB^{-1})B = RBP \quad (2.28a)$$
$$\eta_1^2 x_1^2 + \eta_2^2 x_2^2 + \eta_3^2 x_3^2 = 1 \quad \text{equivalent to } P_1 = I + d_1 p_1' \quad (2.28b)$$
$$x_1 + x_3 = 0$$

From these equations, two solutions for x_i are obtained: x_{i1} and x_{i2}.

Let a unit normal $n_i' (n_1, n_2, n_3)$ be the invariant normal. The Bain distortion then causes n_i' to transform to $\underline{n}_i' = n_i' B^{-1}$. As the $\underline{n}_i'$ is unchanged in length, $\underline{n}_i' \underline{n}_i = n_i' B^{-2} n_i$. In addition, $n_i' d_2 = 0$ because the plane with normal n_i' does contain the shear direction d_2. Assuming that d_2 is parallel to $[\bar{1}\ 0\ 1]$, one obtains the following three equations for n_i':

$$n_1^2 + n_2^2 + n_3^2 = 1$$
$$\frac{n_1^2}{\eta_1^2} + \frac{n_2^2}{\eta_2^2} + \frac{n_3^2}{\eta_3^2} = 1 \qquad (2.29)$$
$$-n_1 + n_3 = 0$$

From these equations two solutions for n_i' are derived, viz. n_{i1}' and n_{i2}'

Four combinations of x_i and $n_i^{'}$ are possible. From these four, one combination will be taken for numerical calculations.

2.2.11.4. The Bain distortion

The Bain distortion is represented by the matrix B:

$$B = \begin{bmatrix} \eta_1 & 0 & 0 \\ 0 & \eta_2 & 0 \\ 0 & 0 & \eta_3 \end{bmatrix} \qquad (2.30)$$

$$\underline{x}_i = Bx_i$$

Now $p_2^{'}$ transforms to $p_2^{'}B^{-1}$ due to the Bain distortion. Considering the normalized $\underline{p}_2^{'}$, one finds

$$\underline{p}_2^{'} = p_2^{'}B^{-1} / \left(p_2^{'}B^{-2}p_2\right)^{1/2} \qquad (2.31)$$

$\underline{x}_i$ is seen to lie in the plane with normal $\underline{p}_2^{'}$, because $\underline{p}_2^{'}.\underline{x}_i = 0$

2.2.11.5 Calculation of the invariant line strain S

The invariant line strain S can be calculated if the rotation matrix is known, with which both $\underline{x}_i$ and $\underline{n}_i{'}$ rotate back to the initial positions, x_i and $n_i^{'}$. Such a rotation matrix can be obtained in principle by solving two equations, $R_0\underline{x}_i = x_i$ and $\underline{n}_i^{'}R_0^{-1} = n_i^{'}$, and using the properties of an orthogonal matrix. But in practice, solving these equations is not necessarily easy. A more convenient method is used to obtain the invariant line strain as follows:

The first step is to obtain a rotation matrix that transforms $\underline{x}_i$ to x_i and the second is to obtain a rotation matrix that leaves x_i unchanged and transforms $\underline{n}_i{'}$ to $n_i^{'}$. The former matrix can be expressed as the product of a rotation matrix R_1, whose elements in the first column coincide with the components of x_i, by another rotation matrix $R_2^{'}$, whose elements in the first row coincide with the components of $\underline{x}_i$. Though the other elements of the rotation matrices, R_1 and $R_2^{'}$, are arbitrary, their three-component vectors must satisfy the orthogonal conditions. As component vectors satisfying these conditions, p_2 and $\underline{p}_2$ will be chosen for R_1 and R_2 respectively. Then one obtains:

$$R_1 = \left(x_i, p_2, u\right),$$
$$\text{where} \qquad u = x_i \times p_2$$
$$R_2 = \left(\underline{x}_i, \underline{p}_2, v\right),$$

where $v = x_i \text{ x } \underline{p}_2$

$R_1 \times R_2^{'}$ is a rotation matrix that makes x_i rotate back to x_i. In other words, the matrix defined by $S_{(0)} = R_1 \times R_2^{'} \times B$ has x_1 as an invariant line. In order to obtain a rotation matrix that makes the $\underline{n}_1$ transform to $\underline{n}_1'$ and x_1 remain unchanged, it is convenient to convert the basis to a new i basis (i_1 i_2 i_3) defined by three orthogonal vectors x_1, p_2 and u.

In the i basis $S_{(0)} = R_1 \times R_2^{'} \times B$ can be rewritten as $(iS_{(0)}i) = R_2^{'} \times B \times R_1$.
Then, the invariant line strain S referred to the i basis (iSi) is obtained by adding a rotation of β around x_1; that is,

$$\left[1 \quad 0 \quad 0,0 \quad \cos\beta \quad -\sin\beta,0 \quad \sin\beta \quad \cos\beta\right] \times R_2^{'} B R_1 = (iSi)$$

$$\begin{bmatrix} 1 & 0 & 0 \\ 0 & \cos\beta & -\sin\beta \\ 0 & \sin\beta & \cos\beta \end{bmatrix} R_2^{'} B R_1 \equiv (iSi) \qquad (2.32)$$

The value of β must be chosen so that $n_i^{'}$ remains unchanged after it is operated on by (iSi). When $n_i^{'}$ is referred to the I basis, that is,

$$\begin{aligned} n_{1i} &= n_1^{'} R_1 \\ iS_0 i &= R_2^{'} B R_1 \\ (n_i^{'}; i) &= n_i^{'} R_1 \end{aligned} \qquad (2.33)$$

The following equation must hold:

$$(n_i^{'}; i)(iSi) = (n_i^{'}; i) \qquad (2.34)$$

From these equations β can be determined. That is substituting equations (2.32) and (2.33) into (2.34).

$$Q = \begin{bmatrix} 1 & 0 & 0 \\ 0 & \cos\beta & -\sin\beta \\ 0 & \sin\beta & \cos\beta \end{bmatrix}$$

$$(iSi) = QR_2^{'*} B R_1 = \begin{bmatrix} 1 & 0 & 0 \\ 0 & \cos\beta & -\sin\beta \\ 0 & \sin\beta & \cos\beta \end{bmatrix} R_2^{'*} \begin{bmatrix} \eta_1 & 0 & 0 \\ 0 & \eta_2 & 0 \\ 0 & 0 & \eta_3 \end{bmatrix} R_1 \qquad (2.35)$$

The shape strain matrix is then given by:

$$S = R_1(iSi)R_1^{'} \qquad (2.36)$$

2.2.11.6. Calculation of the total shape change P_1 and the complementary shear P_2

The invariant plane normal $p_1^{'}$ in the shape deformation is parallel to $p_2^{'}S^{-1} - p_2^{'}$. The normalised vector is $p_1^{'}$ and D is parallel to $p_1^{'}$. The Displacement Vector d_1 of the shape deformation is equal to:

$$(Sd_2 - d_2)/(p_1'd_2). \qquad (2.37)$$

where y is an arbitrary vector lying in the plane with normal $p_1^{'}$.
Then, choosing y to be the cross product $[1 \quad 0 \quad 0]$ x p_1:

$$d_2 = (y - yS^{-1})/(p_2^{'}y') \qquad (2.38)$$

Thus, d_1 is not a unit vector. From the normalisation factor for this vector, the magnitude of the shape deformation can be obtained:

$$m_1 = norm(d_1) \qquad (2.39)$$

From the normalisation factor for d_2, the magnitude m_2 and the shear angle α of the complementary shear can be obtained through:

$$\begin{aligned} \lambda_1 &= \eta_1 \\ \lambda_3 &= 1 \\ \lambda_2 &= \eta_1.\eta_3 \\ s &= \left[(\lambda_1^{\,2} - 1)(1 - \lambda_2^{\,2})\right]^{1/2} \\ m_2 &= s/(\lambda_1\lambda_2) \\ \alpha &= a\tan(m_2/2) \end{aligned} \qquad (2.40)$$

2.2.11.7. Calculation of the orientation relationship

2.2.11.7.1 Kurdjumov – Sachs

The total shape change P_1 associated with the transformation is equal to SP. Since P is not accompanied by any change of crystal orientation, the orientation relationship is determined only by S. According to the Bain correspondence, $(1 \quad 1 \quad 1)_f$ and $[\bar{1} \quad 0 \quad 1]_f$ in the austenite lattice correspond to $(0 \quad 1 \quad 1)_b$ and $[\bar{1} \quad \bar{1} \quad 1]_b$, respectively in the martensite lattice. The $(1 \quad 1 \quad 1)_f$ plane should be transformed by S to $J = [1 \quad 1 \quad 1]$. The $(1 \quad 1 \quad 1)_f$ plane should be transformed by S to $(1/\sqrt{3})(1 \quad 1 \quad 1)S^{-1}$. The unit normal of the transformed $(1 \quad 1 \quad 1)_f$ plane is u_1. u_1 should be a unit vector parallel to the normal of the $(0 \quad 1 \quad 1)_b$ plane.

Therefore, the scalar product of the normal of the $(0\ \ 1\ \ 1)_b$ plane and that of the original $(1\ \ 1\ \ 1)_f$ plane is the cosine of the angle between $(1\ \ 1\ \ 1)_f$ and $(0\ \ 1\ \ 1)_b$. Next, $[\bar{1}\ \ 0\ \ 1]_f$ is transformed by S to $S[\bar{1}\ \ 0\ \ 1]_f$. By normalizing this, we obtain a unit vector parallel to $[\bar{1}\ \ \bar{1}\ \ 1]_b$. From the scalar product of this unit vector with that of $[\bar{1}\ \ 0\ \ 1]_f$, the angle between $[\bar{1}\ \ 0\ \ 1]_f$ and $[\bar{1}\ \ \bar{1}\ \ 1]_b$ is obtained. The non-parallelism indicates that the K-S relation does not hold exactly.

2.2.11.7.2. Nishiyama Wasserman

Use similar calculations regarding the $[\bar{1}\ \ \bar{1}\ \ 2]_f$ direction and the corresponding $[0\ \ \bar{1}\ \ 1]_b$ direction.

2.3. Tempered martensite and its mechanical properties

Generally mechanical properties of a material are determinable (at least in principle), if its microstructure is known in detail. The crystal structure and the chemical composition of the phases in the microstructure are important factors for the mechanical, physical, and chemical properties. Volume fraction, shape, arrangement, and orientation of microstructural constituents are less important for the chemical properties, where constituents can be compared (e.g. in their corrosion resistance). In some cases, such as intercrystalline corrosion or high temperature corrosion, the phase boundaries and the chemical composition of the surrounding matrix must be taken into account. Volume fraction, shape, arrangement, and phase orientation in a microstructure have a greater influence, however, on the physical and mechanical properties. In the different microstructures, the strengthening mechanisms in steels – strengthening by solid solution, dislocations, second phase particles and grain size – are superimposed. Additional effects arise from the arrangement of second phases.

2.3.1 Effect of Carbon additions

In steels, the Carbon content of the alloy will have a significant effect on the hardness of martensite. At too high a value of Carbon, retained austenite will appear and the macro-hardness of the alloy will decrease once more. It appears that the hardness of martensite is a linear function of the square root of the Carbon content. These results are a summary of a large number of investigations [72,73] that also include low alloy steels where the tensile strength of a martensitic steel obeys the following equation:

$$\sigma_M = \sigma_M^0 + K_M \sqrt{C_M}$$

where σ_M^0 and K_M are constants and C_M is the mass percent of Carbon in the steel. This relationship is, of course, only valid if the alloy contains 100% martensite. If this is not the case, then a weighting factor needs to be introduced. Such a relationship is of particular use in martensitic/austenitic dual phase steels.

2.3.2 Effect of Sulphur and Manganese content

There is abundant [74], evidence that reducing the inclusion volume fraction by lowering Sulphur levels to the minimum possible, will improve the upper shelf fracture energy and the impact toughness of the steel. In some cases such data have been interpreted in terms of sulphide spacing and shape and their impact has been primarily the motivation in the production of cleaner steels with very low Sulphur levels. Today, Ultra High Strength steels can be produced with Sulphur levels of the order of 0.003wt %S, or even lower. The Rice and Johnson model [in 74] suggests that the upper shelf fracture toughness of ultra high strength steels should scale as the square root of the sulphide spacing.

Implicit in the second approach to the design of ultra high strength steels is the assumption that appropriate modifications to the microstructure by changes in composition, heat treatment or both, can be found which will improve the toughness of the steel. Empirical knowledge has been gained which suggests that the microstructural features that influence the toughness, include prior austenite grain size, martensite packet size, the amount, morphology and mechanical stability of retained austenite, the size, spacing, shape and coherency of particles precipitated upon tempering, as well as the relative amounts of dislocated and plate-shaped martensite. The proposed model of Garrison [in 74] suggests that at the point of fracture initiation the crack tip opening displacement will scale as the product of two terms – one being the sulphide spacing and the other a measure of localised ductility lacking in the Rice and Johnson model. The data to date suggest that it is through this measure of localised ductility that the microstructure influences the toughness of the steel. This implies that two distinct alloy design methodologies are possible, one to maximise the sulphide spacing and the other to maximise the localised ductility through control of the microstructure.

The critical crack tip opening displacement, δ_{IC} , can be related to the fracture toughness, through the equations:

$$\delta_{IC} = d_n \frac{J_{IC}}{\sigma_0} \qquad (2..41)$$

$$J_{IC} = \frac{K_{IC}{}^2}{E'} \qquad (2.42)$$

$E' = E$ for plane stress conditions and $E' = \frac{E}{(1-\nu^2)}$ for plane strain conditions where E is Young's modulus, σ_0 is the average of the yield strength and ultimate tensile strength, ν is Poisson's ratio, and d_n is a function of the yield strain, K_{IC} is the fracture toughness, J_{IC} is the area specific energy for crack propagation, and whether plane stress or plane strain conditions are assumed. The plane strain fracture toughness should scale E' as:

$$K_{IC} \approx \left\{ \frac{X_0 (R_V / R_l) \sigma_0 E}{d_n} \right\}^{1/2} \qquad (2.43)$$

This approach predicts the same dependence on X_0, the primary particle spacing, as the Rice and Johnson model, but (R_V / R_l) introduces a measure of the ductility lacking in that model. R_l is the radius of primary particles assumed to be spherical sulphide and R_V is the void radius. This model has been applied to several ultra high strength steels for which the primary particles are spherical sulphides. The average three-dimensional nearest neighbour distance between sulphides, X_0, is been calculated from [74]:

$$\frac{X_0}{R_0} = 0.89 f^{-1/3} \qquad (2.44)$$

where f is the sulphide volume fraction and R_0 the average sulphide radius.

From formulas (2.41) to (2.44) there appears to be an excellent correlation between δ_{IC} and the quantity $X_0 (R_V / R_l)\big|_{R_0}$. However, the factors which determine $(R_V / R_l)\big|_{R_0}$ are not really known. According to the model, $(R_V / R_l)\big|_{R_0}$ will continue to increase in accordance with the stress-strain history until the voids nucleated at sulphides coalesce through processes of void sheet coalescence, strain localisation or both. There is clear evidence that the microstructure can influence $(R_V / R_l)\big|_{R_0}$. However, a number of other factors could also influence this parameter. Presumably these include the yield strength and work hardening capacity as both influence flow localisation. In addition, while manganese sulphides are believed to be weakly bound to the matrix, it is possible that the nucleation strains as well as spatial and size distributions of the sulphides could influence $(R_V / R_l)\big|_{R_0}$. The influence of microstructure on $(R_V / R_l)\big|_{R_0}$ is most clearly illustrated by considering the effect of tempering on the toughness. From the equation $\frac{X_0}{R_0} = 0.89 f^{-1/3}$, X_0 can be increased by increasing R_0, the average sulphide radius, or by reducing the sulphide volume fraction f, which in effect reduces the sulphur content. While X_0 can be increased by reducing f, the fracture toughness will scale as $f^{-1/6}$ if R_0 remains unchanged. However, if R_0 is increased without changing f, the fracture toughness will scale as $R_0^{1/2}$.

The strong dependence of fracture toughness on R_0 suggests that by increasing the average sulphide size – that is, by replacing a dispersion of fine closely spaced sulphides by larger more widely spaced sulphides – significant improvements in toughness can be realised. Even if Sulphur levels are reduced to very low levels ($\cong 0.001 wt\%$ S), it should be possible to achieve further improvements in toughness by increasing X_0 through R_0. At a sulphide spacing of about $10\,\mu m$, low alloy quenched and tempered steels can achieve a fracture toughness of 115 MPa(m)$^{1/2}$ at a yield strength of about 1700 MPa [74]. Significant further improvements in toughness of such steels will require sulphide spacing of the order of 20 – 30 μm. The only way sufficiently large sulphide spacing can be obtained is by reducing sulphide volume fractions to the minimum level possible and then increasing the average size.

Therefore, the application of this methodology for improving toughness reduces to the problem of maximising, for a given sulphide volume fraction, the average size.
The methods utilised in achieving this goal will depend on the nature of the sulphides present in the steel. If sulphides are Manganese sulphides then it is suggested that maximum sulphide size, and hence spacing, can be achieved by integrated application of three strategies. The first is the control of sulphide shape and size in the as – cast condition with the goal being equiaxed sulphides of the largest possible size. The second is to utilise forging techniques, which minimize elongation of the sulphides in the as-cast structures. The third is to coarsen the sulphide distribution after forging [74].

On solidification, three primary sulphide morphologies are observed [74]. Type I sulphides are spherical and are favoured by high Oxygen and low Carbon levels. Type II sulphides are often dendritic, rosette-like or fan-like in form, and are favoured by low Oxygen levels. Type III sulphides are faceted equiaxed particles and are favoured by low Oxygen levels in combination with high Carbon levels, Silicon additions and Aluminium additions. There is also an influence of Sulphur content on sulphide type, with type III sulphides favoured as the Sulphur content is reduced. Cooling rate on solidification can influence the sulphide type. Type II sulphides are favoured over both type I and type III sulphides as the cooling rate is increased. It is agreed [74] that type II sulphides form as a result of the eutectic reaction $L \rightarrow Fe + MnS$. Type III sulphides, because of their faceted form, are believed to precipitate as a solid in the interdendritic liquid. However, Type III sulphides seem to be more uniformly distributed than type II sulphides [74]. This could be attributed to their precipitation in the liquid at higher temperatures than Type II sulphides and their entrapment by growing dendrites. The most useful compositions should be those, which promote Type III sulphides.

There have been numerous studies [74] of the effects of temperature and extent of deformation during hot rolling on the shape and morphology of manganese sulphides. During hot rolling the rod-like type II sulphides become aligned parallel to the rolling direction and type I and type III sulphides become elongated plates, lengthening primarily parallel to the rolling direction. The extent of this elongation is minimised by rolling at the highest possible temperatures. In general it has been found that type III sulphides are more plastic than type I sulphides and elongate during rolling to a greater extent [74]. This has been attributed to the higher Oxygen content of type I sulphides. However, upset and cross forging could alter this simple description. Rolling would orient the rod-like Type II sulphides parallel to the rolling direction and elongate Type III sulphides in the direction of rolling. However, upset and cross forging could break up the Type II sulphides and possibly preserve the equiaxed nature of the Type III sulphides. In that case, after upset and cross forging, the sulphides precipitated as Type II and Type III, would now consist of small broken fragments and larger equiaxed particles respectively.

2.3.3. Effect of alloying elements

Tanino and co-workers [26] have shown that Mo moderately increases the yield strength of martensitic steels, probably due to its large atomic size, whereas the addition of Mn results in a slight decrease in yield strength. Schramm et al. [2] reported that both Mn and Mo increase the stacking fault energy of the austenite matrix, although Mn is generally considered to stabilize the γ- phase by lowering the stacking fault energy of the austenite.

Carbon is considered to increase the stacking fault energy of the austenite matrix [73]. The strengthening of the austenite matrix will require a larger driving force for its decomposition to martensite, giving rise to a decrease in M_s temperature. Silicon has an incredibly small solubility in cementite. Therefore, increasing the Silicon concentration of a steel to a value greater that about 1.5 wt%Si ensures the absence of cementite in upper bainite [75]. Interlath cementite in bainite is responsible for initiating fracture in high-strength steels. Its absence is, therefore, expected to make the microstructure more resistant to cleavage failure and void formation.

The ductile films of austenite, which usually are intimately dispersed between the plates of martensite, have a blunting effect on crack propagation. They further add to the toughness by increasing the energy of fracture as the austenite is induced to transform to martensite under the influence of the stress field of a propagating crack. This is the TRIP effect, or transformation induced plasticity effect.

2.3.4. Ageing of Iron – Carbon martensite at room temperature

The details of Carbon partitioning during or after displacive or martensitic transformation are still somewhat controversial. In martensite, the displacive transformation is usually believed to occur without diffusion of Carbon or interstitials [41], and thus the body – centred martensite phase can be substantially saturated with Carbon. Subsequent Carbon partitioning between martensite and retained austenite is not considered because the temperature is too low for substantial amounts of diffusion to occur after quenching, and because Carbon supersaturation is usually eliminated by competing processes, e.g. carbide precipitation during tempering [59]. There is, however, evidence that Carbon partitioning from martensite to retained austenite does occur to thin interlath films during cooling [26] or by isothermal holding in a Si-containing steel after transformation [76].

Carbon partitioning is one means of stabilizing austenite against further transformation at lower temperatures, and is likely to be especially important in these steels containing alloying additions (e.g. Silicon) that suppress formation of Iron carbides [77].

2.3.5. Low temperature tempering of Martensite

Generally, quenching and tempering are well-established means to produce strengthening in steel, which can be achieved mainly due to the precipitation of a fine dispersion of alloy carbides during tempering at elevated temperatures [72]. Known for forming the highest level of strength in steel, the martensite structure is rarely used in an untempered condition because a large number of internal stresses associated with the transformation cause the material to be lacking in ductility [2,78]. However, low-temperature tempering is sufficient to reduce these stresses considerably without changing the basic features of the martensite structure. Therefore, from the commercial point of view, the study of martensitic steels has to include that of steels tempered in the range of 200-250 ^0C. However, apart from the effect of tempering temperature, the strength of the martensitic structure is dominated by the Carbon content and volume fraction of martensite and, therefore, is affected indirectly by the M_s and the M_f temperatures [75].

The mechanical behaviour of a quenched-and-tempered steel depends strongly on its microstructure. Thus, the study of the effects of the microstructure and dislocation substructure of a steel on its strength, ductility and fracture characteristics is of great

importance from the viewpoint of both theory and practice. The so-called "first stage" of tempering (T1) is associated with the appearance of a metastable and coherent ε transition carbide, which precipitates uniformly throughout the martensite phase. Although the precipitation of the transition carbide proceeds within a few minutes in the temperature range of 100 to $200\,^{o}C$, precipitation of ε carbides has been detected at temperatures as low as room temperature after several months of aging [78]. Tempering well into the T1 temperature range leads to a dispersion of coarse particles in a matrix of low-Carbon martensite. Above $200\,^{o}C$ the transition carbide is replaced by the more stable Fe_3C and at higher temperatures by the M_3C carbide if substitutional carbide forming alloying elements are present in the steel. This implies diffusion of substitutional alloying elements at the higher temperatures. If the steel is tempered below $200\,^{o}C$ the transformation to cementite would necessitate several months to become effective [78]. The precipitation of cementite marks the third stage of tempering.

2.3.5.1. Structure and Morphology of the Stage 1 Carbide

In his early X-ray investigation, Jack [in 72] found that the Stage 1 carbide in high-Carbon martensite possessed hexagonal symmetry and he called this phase epsilon carbide (ε carbide). Jack's proposed orientation relationship between ε carbide and low-carbon martensite:

$$(0001)_{\varepsilon} \,//\, (011)_{\alpha}$$

and

$$(10\bar{1}1)_{\varepsilon} \,//\, (101)_{\alpha}$$

was confirmed by Wells [in 72] more than 20 years ago and has also been found in numerous other selected-area electron-diffraction studies. Unable to identify the positions of the Carbon atoms in the ε structure, Jack suggested that the ε carbide might exhibit a range of compositions from Fe_2C to Fe_3C. Later calculations based on dilatometry results [78, 79] placed the composition at $Fe_{2.4}C$. The APFIM results of Chang [in 78] on an Fe-15%Ni-1%C martensite tempered at $130\,^{0}C$, indicate a composition of about 20 to 25 at%C. This is close to the M_3C stochiometry, but considerably less than the 33 at% C required for an M_2C carbide. Detailed electron-diffraction investigations of Fe-C and Fe-Ni-C martensites by Hirotsu et al. [in 72] indicated that Carbon atoms may be ordered in the transition carbide, reducing the symmetry from hexagonal to orthorhombic. They referred to the ordered phase as eta carbide (η carbide) to distinguish it from Jack's hexagonal carbide. Taylor [in 72] has suggested that the η carbide can be regarded as a derivative of the ε carbide structure, and that it may be more appropriate to refer to the ordered carbide as "ε'", thereby recognizing its structural similarity to Jack's ε carbide.

A variety of morphologies have been reported for the Stage 1 carbide. Early TEM investigations of Fe-Ni-C martensitic steels [in 72] reported a plate-like carbide with a $\{100\}_{\alpha}$ habit plane. Later work on Fe-Mn-C [in 72] alloys concluded that the carbides were rodlike in shape along $\langle 100 \rangle_{\alpha}$. Other studies of Fe-Ni-C and Fe-Si-C alloys found the carbide particles to be rodlike, but with the long axis nearly parallel to $\langle 211 \rangle_{\alpha}$. To complicate this issue further, several studies employing dark-field electron microscopy [72]

indicated that what appeared to be rodlike carbides were actually composed of arrays of much smaller particles. The disparity among these observations suggests that alloy composition might exert an important influence on the actual carbide morphology.

2.3.5.2 Nucleation and Growth of the Stage 1 Carbide

For many years, Stage 1 carbide precipitation was regarded as a homogeneous process occurring by classical nucleation and growth in a single-phase matrix. However, results on martensite ageing [72] show that a decomposition process precedes the precipitation of T1 carbides, opening up the possibility that structural features of aged martensite influence the mechanism of subsequent Stage 1 carbide nucleation. Nakamura et al. [in 72] have suggested that stage 1 carbides emerge directly from the modulated structure associated with the prior A stage of tempering below room temperature. Nakamura et al., based on their high-resolution TEM imaging results on an Fe-1.5%C alloy, concluded that the Iron-atom displacements produced by interstitial Carbon atoms favour nucleation in the high-Carbon product of the modulated structure. Although the actual mechanism by which Stage 1 carbide nucleation occurs is not yet firmly established, the above results indicate that the nucleation of T1 carbides is heterogeneous, at least in martensites that undergo spinodal decomposition prior to T1 carbide precipitation such as in high Chromium Fe-Cr steels. Macroscopically, precipitation appears to be homogeneous, because the decomposition of virgin martensite occurs uniformly throughout the martensitic phase providing a fine, uniform distribution of sites for subsequent carbide nucleation. New insights into the nature of the growth of the Stage 1 carbide may come from recent results on Fe-Ni-C martensite [72]. What appeared to be stacking faults within platelike carbide particles were observed. These faults appear to represent shearing on the basal plane of the carbide lattice.

In considering the lattice correspondence between ε carbide and the bcc or bct parent phase, Taylor [in 72] demonstrated that the carbide habit plane is macroscopically invariant if a simple shear on the basal plane (representing an internal accommodation deformation mechanism) accompanies the orthorhombic lattice distortion that relates the two structures. Hence, the observed platelike shape of the particles would minimize the strain energy associated with precipitation.

Taylor [in 72] points out that the carbide habit plane and morphology may be composition dependent, inasmuch as the lattice constants (and hence the crystallographic relationship between parent and product phases) are generally a function of alloy composition. This may partly explain the varied carbide morphologies that have been reported. The concept of an invariant-plane strain (IPS) transformation proposed by Taylor has, of course, been widely applied to the diffusionless martensitic reaction in steels. Although the precipitation of T1 carbides is clearly not diffusionless, observations of surface relief produced by Stage 1 tempering on the surfaces of prepolished metallographic specimens [72, 71], indicate that this precipitation has a displacive component. In fact, the net shape strain produced by the bcc $\rightarrow$ ε'-carbide transformation may be responsible for the stress relaxation observed during Stage 1 tempering [72], although other processes such as twinning and detwinning in the martensite phase may also operate. Evidence is accumulating that the IPS mechanism may be at play in reactions that are both displacive and diffusive in nature [72], at least when a lattice correspondence between the parent and product phases can be defined.

2.3.5.3. Kinetics of Stage 1 precipitation

The kinetics of Stage 1 carbide precipitation have been measured in a number of investigations [72]. However, overlap between the A stage (spinodal decomposition of the martensite) and the T1 stage generally complicates the interpretation of the data. Consequently, the rate-controlling mechanism(s) are still not well understood. In general, apparent activation energies in the range of 100 to 150 kJ/mol have been reported [72, 74]. These values are well above the activation energy for Carbon-atom diffusion in body-centred Iron. It has been suggested that carbide precipitation involves the short-circuit diffusion of metal atoms along dislocations, with an activation energy of about 140 kJ/mol. Such diffusion was invoked for the accommodation of growing particles through plastic deformation of the martensitic matrix [77]. However, the proposed IPS transformation suggests that accommodation occurs within the carbide particle, and hence growth would require an intrinsic metal-atom diffusion. Further investigation is required before the factors controlling carbide growth will be completely understood.

2.4. Mechanical properties of tempered martensitic steels

For an alloy steel with the chemical composition;

Elements	C	Si	Mn	Ni	Cr	Mo	P	S
Wt.(%)	0.39	0.24	0.61	1.46	0.67	0.17	0.021	0.006

Woei-Shyan et al. [78] have found the following main results on the tempering of the martensite:

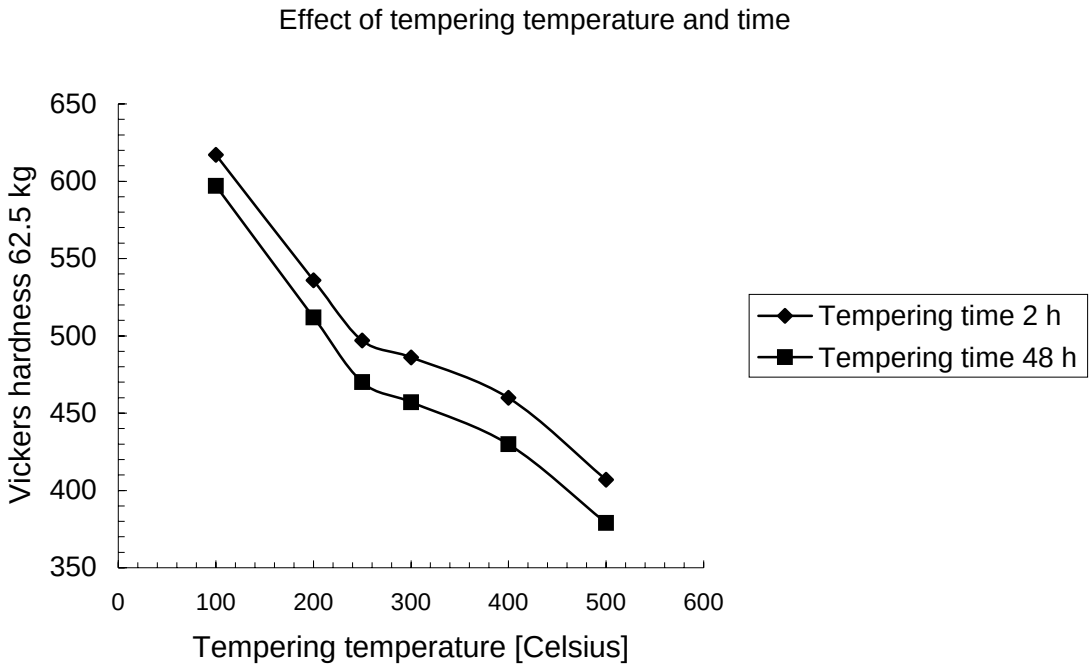

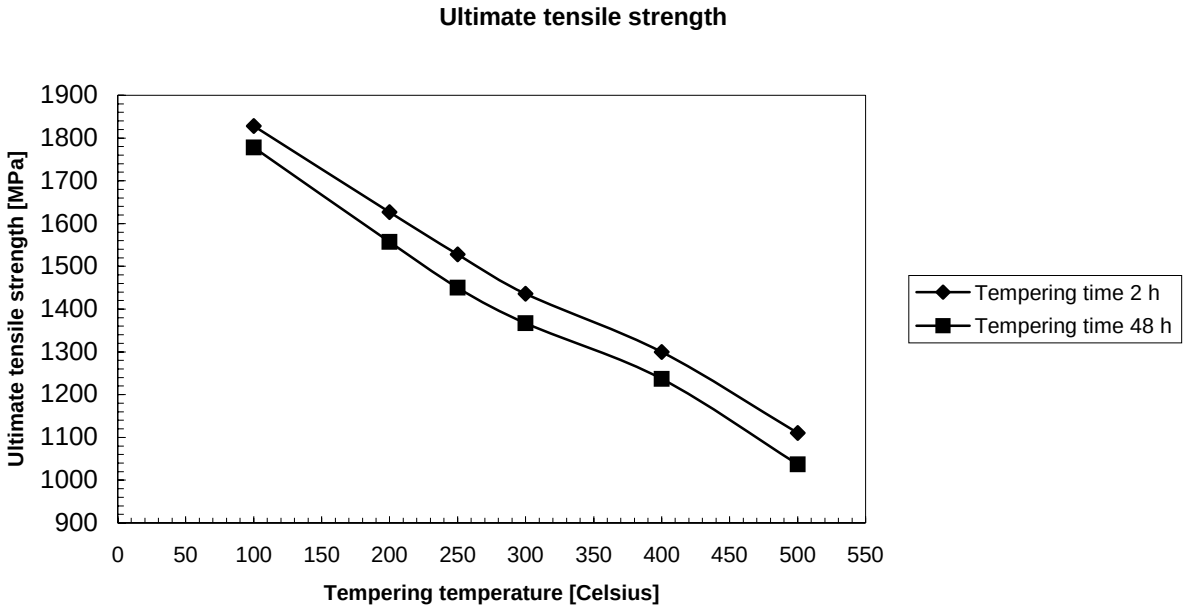

Figure 2.7. Variation of hardness and ultimate tensile strength with the tempering temperature [°C] of a low carbon steel [78]

In the as-quenched condition, the material has the highest level of strength and hardness but its ductility is the lowest, because of the presence of untempered martensite. A large amount of distortion occurs during the formation of the platelets of martensite, which leads to a rapid increase in strength and hardness. The thermal instability of interlath austenite after tempering often leads to the formation of carbide films, which is a fairly general cause of tempered martensite embrittlement [78]. Woei-Shyan et al correlated a loss in toughness after tempering at $300^{0}C$ with the retained interlath austenite and the formation of interlath carbide films that are decomposed from the lath boundary retained austenite.

The study of retained austenite films associated with martensite in low alloy steels has assumed new significance, primarily due to its apparent effect on the mechanical properties of quenched and tempered high-strength steels [51]. Retained austenite has been found even in low-alloy steels with high M_s temperatures after fast cooling to $-196^{0}C$ [80]. Since such refrigeration fails to give a significant decrease in the amount of retained austenite, chemical or thermal stabilization has been ruled out as the possible reasons for the anomalous stability of the retained austenite films [76]. Azevedo and da Silva [in 74] using Mössbauer spectroscopy, and Bhadeshia [77] using X-ray diffraction, observed no evidence for the chemical stabilization by Carbon enrichment of the austenite. While no such enrichment is expected on the basis of the displacive nature of the martensite transformation, partitioning of Carbon is feasible either during the quench (i.e. after formation of some martensite) or during subsequent tempering [75]. Hence, although no direct evidence is available, the stability of the retained austenite has been attributed to mechanical stabilisation [76].

The propensity for austenite retention has been rationalised in terms of the local inter-martensite crystallography, and it was found that twin-related martensite variants do not favour the retention of austenite. Inter-martensite retained austenite films were most profuse when the adjacent martensite variants were in the same crystallographic

orientation [81]. A mechanical stabilisation effect hindered and often prevented transformation to martensite.

Speer and co-workers [95] have recently proposed a thermodynamic model to describe the endpoint of Carbon partitioning between quenched martensite and retained austenite in the absence of carbide formation. This model assumes a stationary α/γ interface, and requires a uniform chemical potential for Carbon (but not for Iron) in the two phases, leading to a metastable equilibrium condition identified as "constrained para-equilibrium" or CPE. In their calculations the authors have shown that the metastable ortho-equilibrium condition between ferrite and austenite cannot be achieved. Consequently they developed a CPE model to predict the endpoint of Carbon partitioning in the presence of a stationary α/γ interface. They have predicted that the austenite inherits most of the Carbon in the steel at constrained para-equilibrium conditions, and the retained austenite can be highly enriched with Carbon in some instances. Applications of CPE partitioning may be considered in steels where carbide formation is suppressed (e.g. with Si, Al, P, or even Ni additions) [75]. They propose the potential for a new "quenching and partitioning" process, or Q&P, where the resulting martensite/austenite mixtures may be substituted for more conventional carbide-free bainitic microstructures such as high-strength TRIP sheet steels or even austempered ductile cast iron.

2.5. The variations of microstructure with tempering temperature and hold time

Woei-Shyan Lee et al. [78] have used TEM investigations to determine the nature of the structural changes and the dislocation distribution after various tempering processes. Since the M_s of their steel was well above room temperature, this has led to autotempering behaviour in the as-quenched structure. Thus, in the case of quenched martensite there are some brief periods in which Carbon atoms can redistribute themselves. Because the stress fields in the lath martensite are situated around individual dislocations and cell walls, certain interstitial lattice sites near to these places, such as defects, provide lower energy positions for Carbon than the normal sites. Such migration can be detected by metallography or by a smaller contribution of Carbon to electrical resistivity or to internal friction, if comparing the Carbon situated in an interstitial site near to a dislocation with that in a "normal" one [82]. Autotempered precipitates were not present in any of the twinned plates but were only resolved in the dislocated laths and untwinned plates formed at lower temperatures, i.e. near to M_f. Tempering involves many different basic processes, such as the precipitation of carbides, the decomposition of retained austenite, and the recovery and recrystallization of the martensite substructure. In the case of Woei-Shyan et al. [78], epsilon carbide ($Fe_{2.4}C$, hcp) was the carbide precipitated when the material was tempered at 200^0C for 2 h. This result confirms fully that of Jack [in 72], but differs from that of Hirotsu et al.[in 72], who found that for martensitic high-Carbon steel, the carbide precipitated during the first stage of tempering is eta-carbide or neta-Fe_2C. The material's microstructure at this temperature is shown in Figure 2.8.1, in which tangles of high-density dislocations and smaller dislocation cells are the two main characteristics in the dislocation structures. Also, epsilon carbide precipitates can be found at the interfaces between the lath martensite.

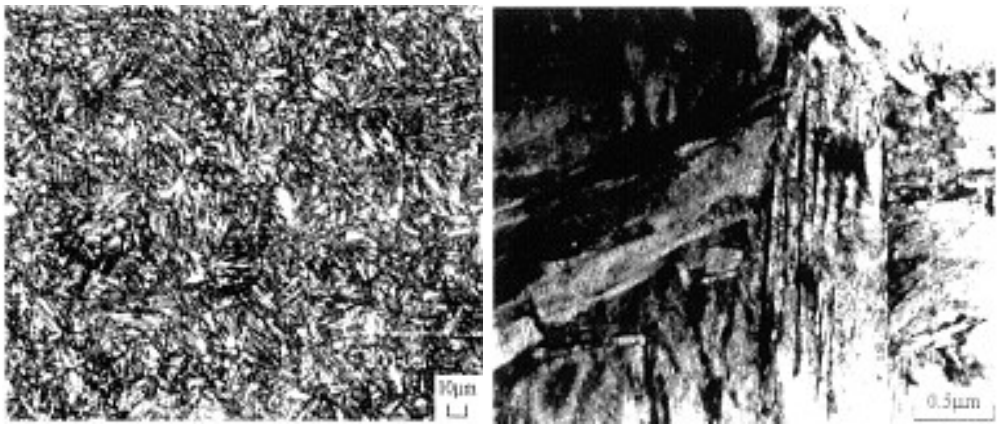

(a) (b)

Figure 2.8.1. (a) Optical micrograph and (b) TEM thin foil of an Fe – 0.2%C specimen quenched in oil ($850^{0}C$ /30minutes) [72].

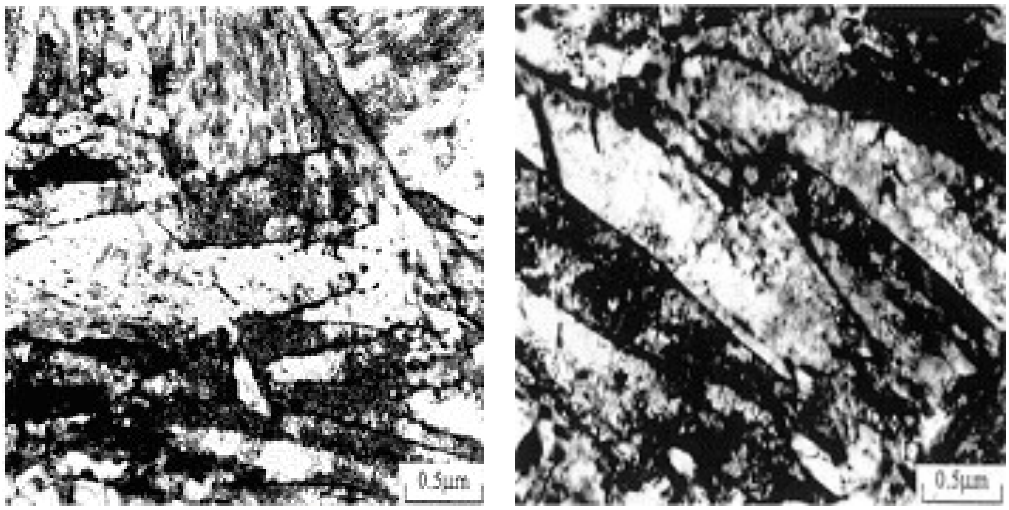

(c) (d)

Figure 2.8.1. (c) TEM micrograph of an Fe – 0.2%C specimen tempered for 2h at $200^{0}C$ and (d) tempered 48h at $200^{0}C$ [72].

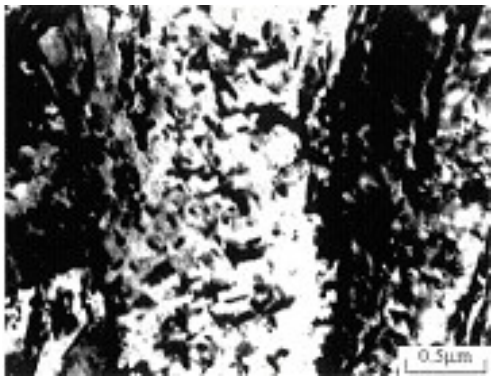

(d)

Figure 2.8.1 (e) TEM micrograph of an Fe – 0.2%C specimen quenched in oil ($850^{0}C$ /30min) and tempered for 2h at $300^{0}C$ [72].

For the case of material tempered at 200°C for 48 h, the observation by transmission electron microscopy shows that some laths have grown larger. Two operating mechanisms should be involved in lath growth. One is the movement of lath boundaries and the other is the elimination of lath boundaries due to the movement and annihilation of dislocations at the boundaries. In this tempered condition, a high density of dislocations with precipitated carbides on them, are present in most of the laths. These carbides immobilise the dislocations and these cannot form dislocation arrays with a low energy as with small-angle grain boundaries. During tempering of this steel at 300°C for 2h, the nucleation sites of the carbides at low temperatures are frequently martensite lath boundaries and at higher temperatures, ferrite grain boundaries. Pietikainen [85], found similar results than Woei-Shyan and Tzay-Tian Su [78] using a steel with the chemical composition;

Element	C	Si	Mn	P	S	Cr	Ni	Mo	V	Cu	Al
Content	0.43	0.28	0.70	0.012	0.025	1.054	0.201	0.179	0.007	0.130	0.017

Pietikainen [85] austenitised the Charpy specimens (without notches) and the tensile specimens at $855^{0}C$ for 30 minutes. The specimens were tempered for 1 hr and for 1s in salt baths and the grain size of the austenite was about ASTM No 7. The main results from their study are presented in Figure 2.9. Pietikainen observed that on the fracture surface of the specimens tempered at $200^{0}C$, about 20% of the intergranular fracture face occurred along former austenite grain boundaries. This kind of fracture was near the hinge area of the Charpy specimen. At a tempering temperature of $100^{0}C$ this type of fracture was rare, as also in the case of a tempering temperature of $280^{0}C$ [85]. No tempered martensite embrittlement during the short tempering time is evident in the figure but with some embrittlement appearing after the 1 hour tempering times.

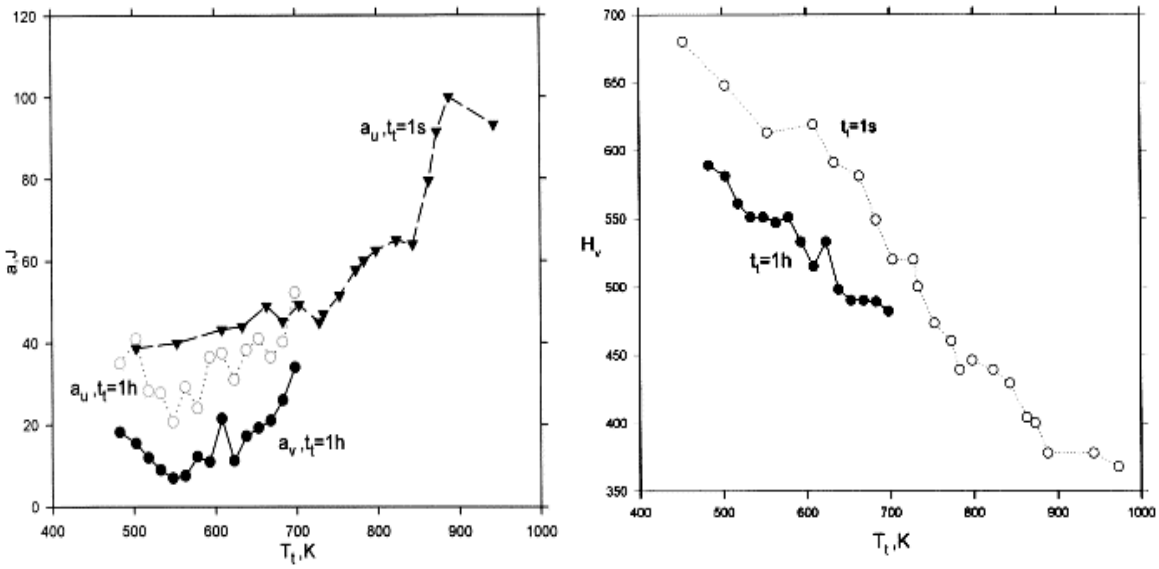

a) b)

Figure 2.9. a) Charpy impact energy U-notch a_u and V-notch a_v , b) Vickers hardness as functions of the tempering temperature [85]

Nakashima and Libsch [86], reported that the Fe_3C particles already become spherical after short tempering times. They were successful in eliminating the TMB in that way.

It seems that this result supports the models in which the plateau with the TMB-valley is connected with the plate-like Fe_3C and not necessarily with the presence of impurities such as As, P, Sb and Sn on austenite grain boundaries. Mechanical instability was considered to be the reason for the tempered martensite embrittlement. Zia-Ebrahimi and Krauss [87] also concluded that TMB was affected by the microstructure and not necessarily by impurities. They also proposed that the localisation of plastic deformation was the reason for the presence of TMB.

2.6. Diffraction patterns of iron carbides

Bimal et al. [88], have investigated the stability of retained austenite in a low Carbon steel subjected to a low temperature ageing treatment. The diffraction patterns of different iron carbides were analysed to characterise the iron carbides precipitated as a function of the tempering temperature. In their study ε-carbide was found to occur in the austenite phase as a result of enrichment by interstitials during isothermal holding.

Decomposition of the austenitic phase commenced at 200^0C. At 300^0C dislocations were rearranged into parallel arrays. Interfacial dislocations were formed due to the mismatch between the parent austenite and the ferrite product. The ε-carbide gave way to the formation of $\varepsilon'(\eta)$-carbide when the tempering temperature was near and above 400^0C and the $\varepsilon'(\eta)$-carbide particles formed on dislocations. Tempering at 500^0C led to the formation of stable cementite. From their study it seems that the shape of the ε-carbides may be a function of the tempering time, although they did not analyse this aspect. The thin foil micrographs and the Selected Area Diffraction Patterns established after their experiments, are illustrated in the following figures 2.10.1 through to 2.10.6.

In their low Carbon steel martensite was seen to undergo degeneration from a planar arrangement of dislocations at 200^0C, as shown in Figure 2.10.1 (d). The tiny particles that decorated these line defects were identified as $\varepsilon-$carbide by the associated $[012]_\alpha$ direction on the SADP. The orientation relationship from the schematic diagram were found as follows:

$$[2110]_\varepsilon // [012]_\alpha$$
$$(0110)_\varepsilon // (200)_\alpha$$
$$(0001)_\varepsilon // (042)_\alpha$$

The early stages in the decomposition of the blocky austenite and the degeneration of the martensite at 200^0C were also studied.

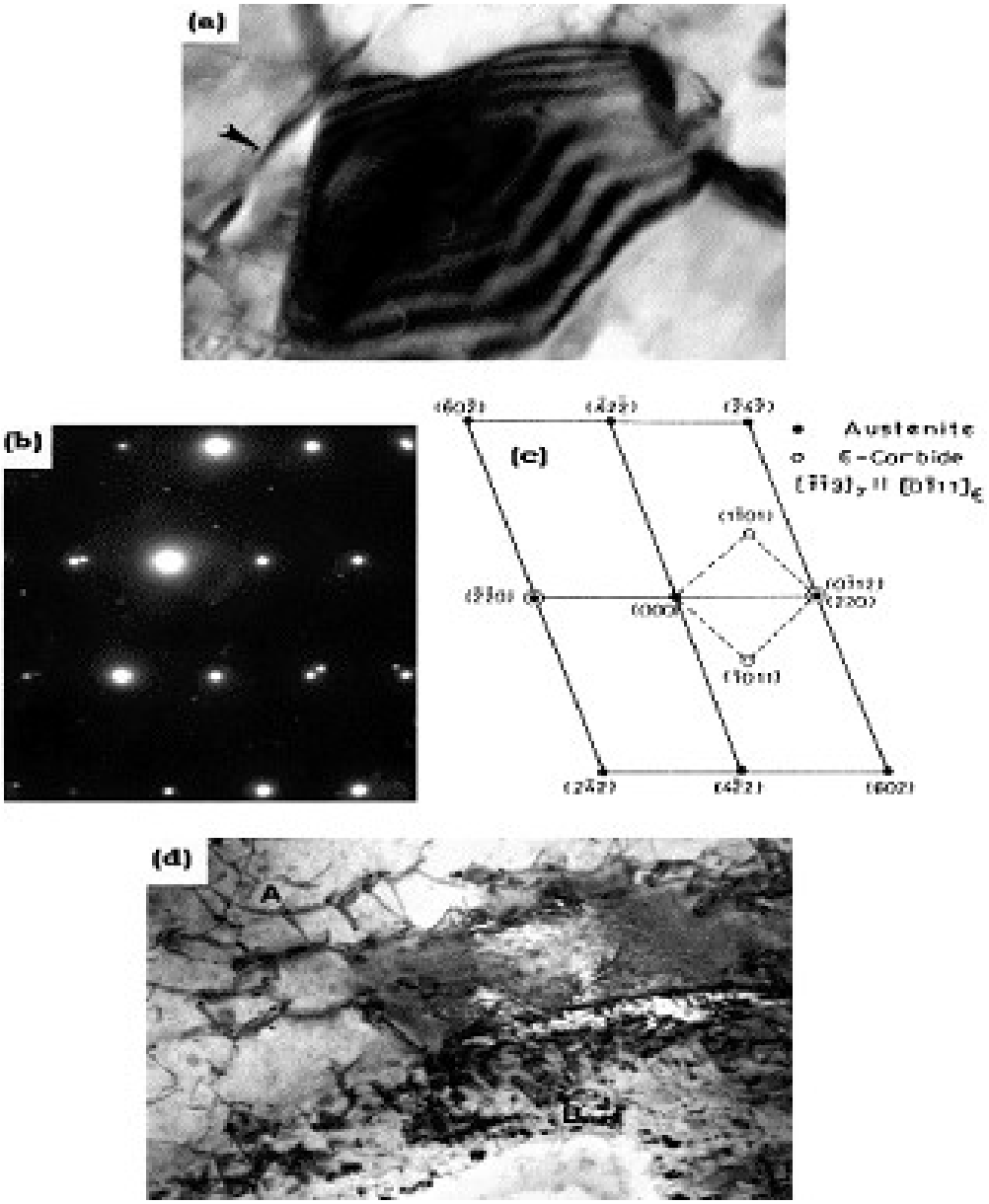

Figure 2.10.1. Transmission electron micrographs of an Fe-0.43%C: a) Bright field electron micrograph revealing blocky nature of retained austenite and the presence of stacking faults as indicated by the arrow. b) Selected area diffraction pattern (SADP) from the same area. c) Schematic representation of the $[113]_{\gamma}$ SADP of Fig. (b) indicating positions of $\varepsilon -$ carbide reflections in austenite matrix. d) Bright field image of the same sample showing generation of partials preceding the transformation (region A) and twinning in martensite (region B). After Bimal et al. [88].

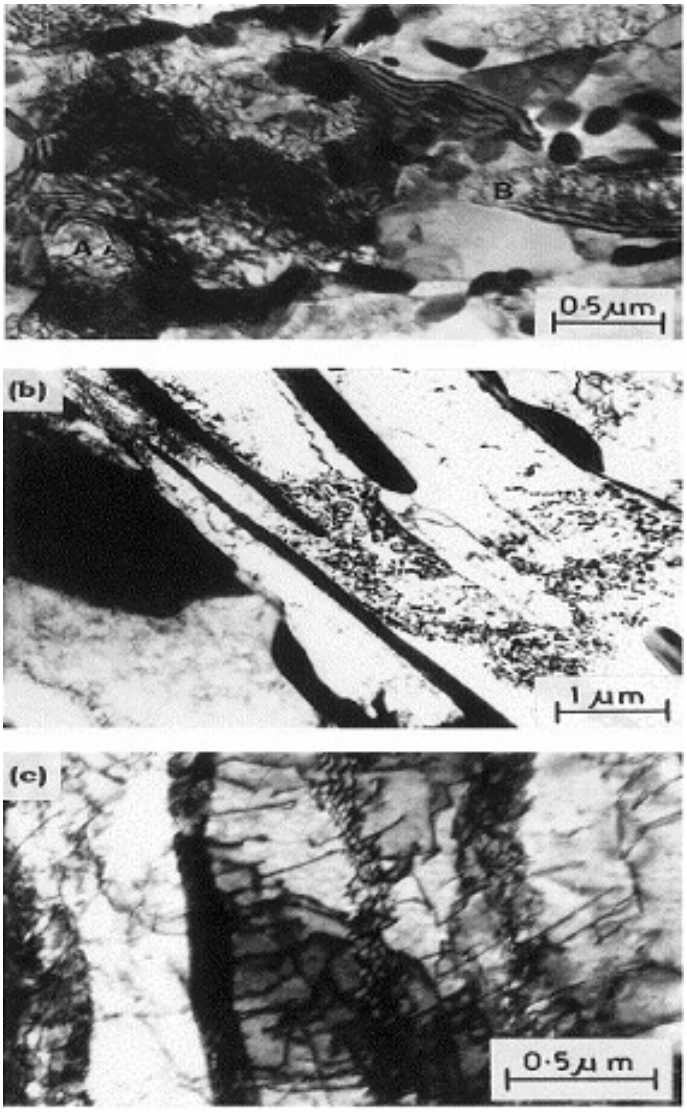

Figure 2.10.2. Bright field electron micrographs from an Fe – 0.43%C sample tempered at $200\,^{0}C$. (a) Early stages in the decomposition of blocky austenite. (b) Film type of austenite in the martensitic regions remain unaffected by tempering. (c) Early stages of degeneration of martensite. After Bimal et al. [88].

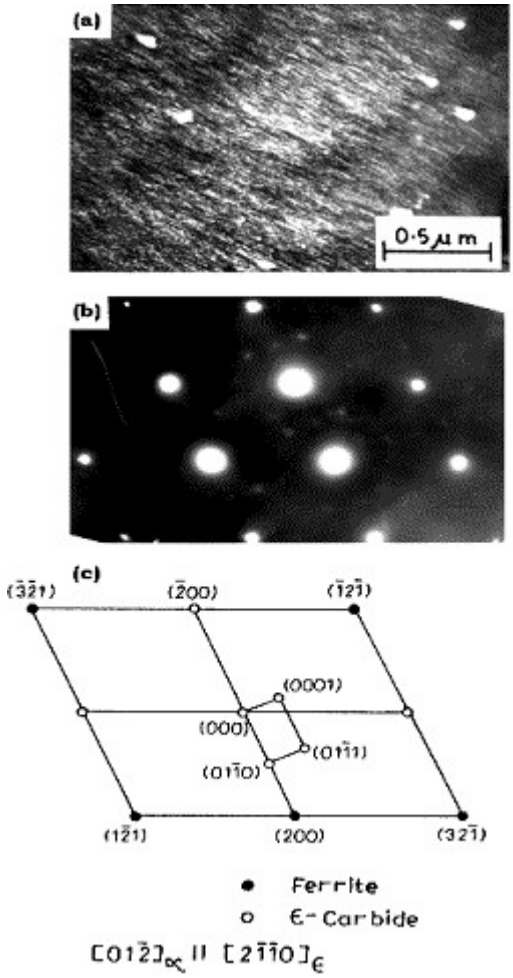

Figure 2.10.3. Transmission electron image from a sample tempered at $300\,^{0}C$. (a) Planar arrays of closely spaced dislocations in ferritic region. Note also the precipitation of fine carbides along dislocations. (b) SADP from the same region. (c) Schematic representation of $[012]_{\alpha}$ SADP of Fig. (b) indicating positions of $\varepsilon-$ carbide reflections in ferritic matrix. After Bimal et al. [88].

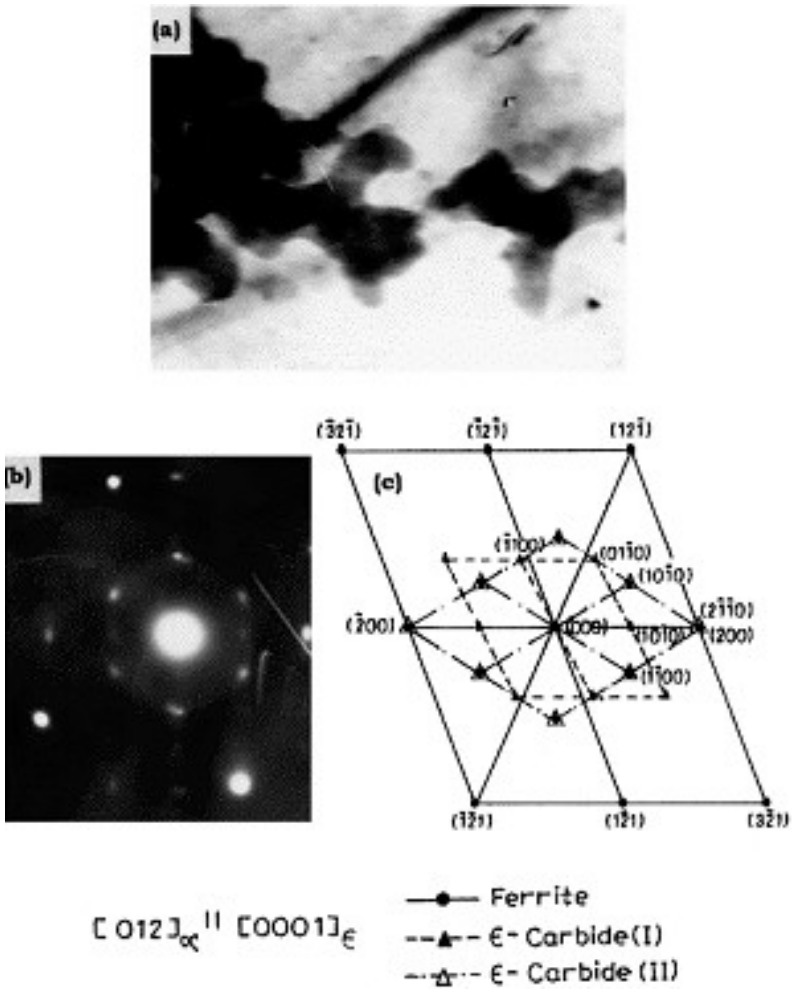

Figure 2.10.4. (a) Bright field electron micrographs showing a three pronged pin-wheel-shaped morphology of $\varepsilon-$carbide precipitate in ferritic matrix. (b) SADP from the same region as in (a). (c) Schematic representation of $[012]_{\alpha}$ of Fig. (b) depicting presence of two domain variants of $\varepsilon-$carbide. After Bimal et al. [88].

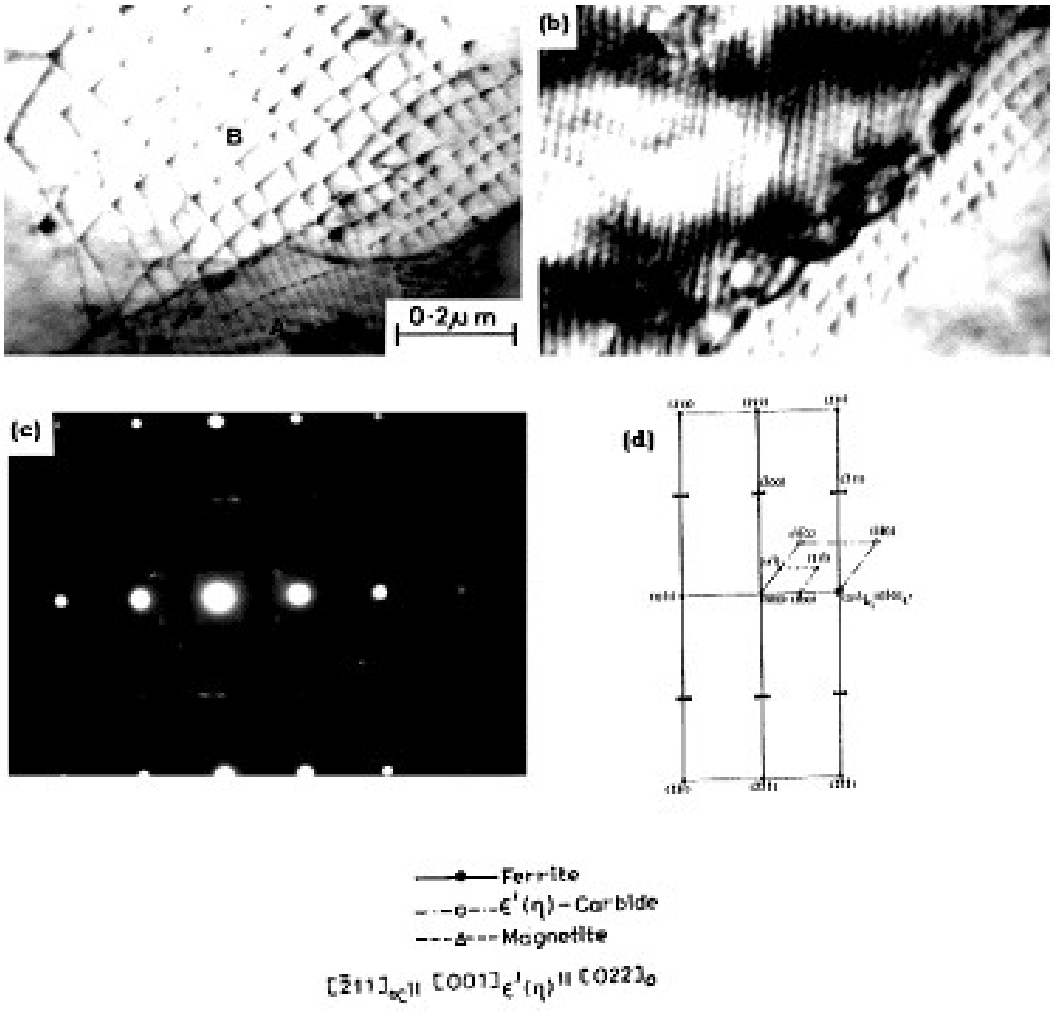

Figure 2.10.5. Transmission electron micrographs from steel sample tempered at $400\,^{0}C$. (a) Bright field showing interfacial structure; (b) precipitation of $\varepsilon'(\eta)$ – carbide along the interfacial dislocation network; (c) SADP from the same region, note the splitting in the $\{200\}_{\alpha}$ and $\{211\}_{\alpha}$ spots; (d) indexed pattern for $[211]_{\alpha}$ indicating locations for $\varepsilon'(\eta)$ – carbide and magnetite reflections. After Bimal et al. [88].

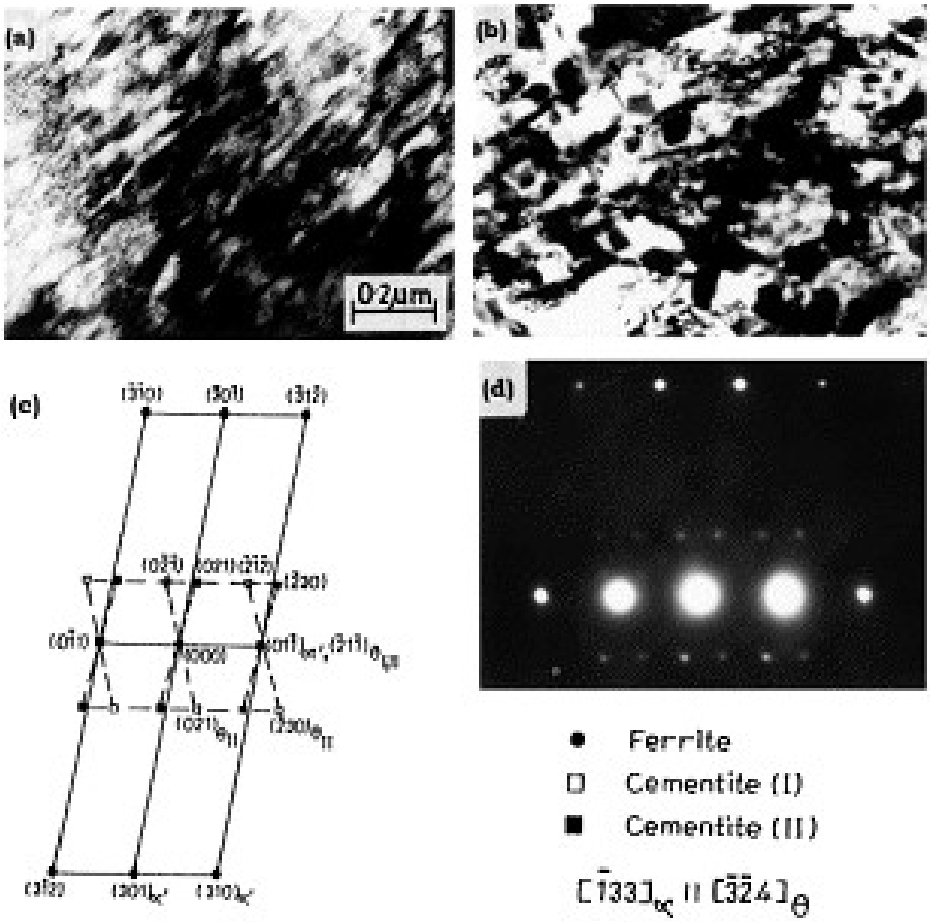

Figure 2.10.6. Transmission electron micrographs from steel sample tempered at $500^{0}C$. (a) parallel arrays of dislocations in the degenerated martensitic region. (b) Formation of coarse cementite particle in he same specimen. 9c) SADP from the same region as Fig. b. (d) Schematic representation of $[133]_{\alpha}$ SADP of Fig. c showing presence of two variants of cementite precipitates. [88].

Thomson and Miller [89] have investigated the partitioning of substitutional solute elements during the tempering of martensite in Cr and Mo containing steels. They observed no partitioning of Cr, Mo and Mn between cementite and martensite after tempering at $350^{0}C$ for 40 hours. The enrichment of Cr, Mo and Mn in the cementite during prolonged ageing at $450^{0}C$ for 187 hours, before the onset of softening, was the same in both the low and high Carbon alloys, with the interface concentration of solute elements rising slowly towards the equilibrium values. Their results provide further support for the theory that cementite precipitates from supersaturated ferrite via a para-equilibrium displacive transformation mechanism. After prolonged ageing at these higher temperatures, significant enrichment of the cementite with respect to the substitutional alloying elements occurs, with a corresponding depletion in the matrix surrounding the carbide. This enrichment at the cementite/matrix interface was not observed to reach the high levels predicted by equilibrium thermodynamics, as they were found experimentally to be the same in cementite in both a low Carbon and a high Carbon alloy with significantly different equilibrium levels of solute elements. This led the authors to conclude that diffusion of the substitutional solutes through the matrix and within the cementite is the rate-controlling step during the early stages of the enrichment process.

The interface concentrations gradually rise from those dictated by para-equilibrium towards the equilibrium concentrations [89].

Interlath austenite was revealed by high resolution lattice imaging electron microscopy from which it was suggested that there was considerable Carbon enrichment at the α'/γ interfaces. Confirmation of this enriched/stabilised interlath austenite was obtained by the powerful atomic resolution method of field atom probe spectroscopy. Heat treatments of α'/γ in the range 300 to $500\,^{0}C$ resulted in austenite decomposing to interlath carbides. The structure became similar to lower bainite, causing embrittlement transgranularly with respect to the prior austenite.[89]

2.7. Tensile properties

Martensite tempered at temperatures between 150 and $200\,^{0}C$ is in the temperature range that defines the first stage of tempering. In this temperature range, fine transition carbides, of the order of 2 – 4 nm in size, precipitate within the martensite crystals [90-91]. Many of the Carbon atoms are tied up in the carbide particles and are, therefore, not available for dynamic strain ageing. Also, the higher the Carbon content of the martensite is, the higher the density and closer the spacing of the transition carbides and the transition carbide clusters [92-93]. Reduced lengths of Carbon-free dislocation segments between the transition carbides would require higher stresses for plastic flow according to the work hardening theory of Kuhlmann-Wilsdorf [in 51]. The theory states that the flow stress τ at any given plastic strain, is given by the equation:

$$\tau = \tau_0 + G_M b/\bar{l}$$

where τ_0 is the friction stress, $\bar{l}$ is the instantaneous average of the active dislocation link lengths, and the other terms have their customary meaning.

2.8. Multiple regression as sequential simple regression

Multiple regression analysis is a useful tool to link a large volume of experimental data with an empirical predictive capability. For example in martensitic alloys, a dependent variable such as the M_s temperature can be linked with an arbitrary number of independent variables such as the weight percentages of the alloying elements. The multiple regression approach consists of regressing a dependent variable y (here the M_s temperature) simultaneously with the independent variables $U_0 = 1$ and x (here the weight percentage of an alloying element) .

The error function is given by:

$$e = y - aU_0 - bx$$

The two regression coefficients a and b are found by the solution of the simultaneous equations:

$$a + b\sum x = \sum y$$
$$a\sum N + b\sum x^2 = \sum xy$$

Solving these simultaneous equations by the most efficient method possible, namely either the Gauss method or its equivalent in the form of the Crout method or the m-reduced array method then, in fact, results in the simple regression approach [94]. This consists of three separate simple regressions, each of them not requiring the solution of simultaneous equations. The first is the simple regression of x on U_0 which yields the net variable

$$x = x - \bar{x} \text{ as the error.}$$

The second is the simple regression of y on U_0 which yields the net variable

$$y = Y - \bar{y} \text{ as the error.}$$

The third simple regression depends upon the results of the first two, and hence the simple regressions must be carried out in a definite sequence in order to build up the multiple regression [94]. Thus multiple regression may be regarded as a sequential simple regression.

CHAPTER 3. EXPERIMENTAL TECHNIQUES

In this part of the work the variables and the techniques used for analysis are presented and rationalised. The choice of the variables and techniques of analysis is based on the hypothesis made in the paragraph 3.1 of this work and on the scientific and industrial backgrounds presented Chapter 2.

3.1. Hypothesis

3.1.1. How to improve the Hardenability and the Hardness

To obtain a Brinell hardness of at least equal to 600 BHN after tempering, as specified by ARMSCOR and Mittal Steel South Africa, one should consider a Carbon content of the alloy above 0.38%C, which is greater than the specified 0.35%C maximum in the current steels A, B, C and D armour plates. The largest effect on the hardenability of the armour plate should arise from the Manganese content of the steel [3]. A compromise should be considered between the hardenability and the final grain size by considering the fact that the large austenite grain size improves the hardenability, but is detrimental to the impact toughness of the final microstructure. Both the homogenisation temperature and time are important parameters as this determines the dissolution of alloying elements in the austenite from pre-existing carbides. The martensite will present the highest hardness in the as-quenched steel. [3]

3.1.2. How to improve the Toughness of the martensite.

The pure martensitic microstructure will be hard and brittle. To achieve the ballistic requirements, i.e. resistance against spalling, a low- temperature tempering treatment is specified. High-temperature tempering above 400^0C is unacceptable for a high ballistic performance as the softening of the steel is accompanied by a high decrease in the hardness, which should be at about 600 BHN as specified. The final ballistic properties will be strongly dependent on both the tempering temperature and time, as well as on the chemical composition of the steel.

3.1.3. How to improve the resistance to Shock and to Spalling

The largest change in DBTT results from changes to the amount of Carbon and Manganese in the alloy. The transition temperature for V- notch Charpy specimens is raised by about $+4^0C$ for each 0.1%C and is lowered by about $-12\ ^0C$ for each 0.1%Mn [74]. Increasing the Carbon content also has a pronounced detrimental effect on the upper shelf impact energy and reduces the weldability of the alloy if that should be considered in manufacturing the armoured vehicle structure. The Mn/C ratio should, therefore, be at least 3:1 for satisfactory notch toughness [2].

3.1.4. How to improve the Tensile Strength

An important development that has resulted in high-strength low-alloy steels with good impact properties is the addition of small amounts of V [73] by causing V_4C_3 precipitates to form during tempering. The dispersion strengthening by this carbide raises the yield strength while at the same time retards grain growth and improves the impact resistance.

3.2. Alloy design

The elements likely to be found in armour steels as well as their potential effects on the microstructure and mechanical properties, are presented in Table (3.1)

Table (3.1). Alloying elements likely to be found in the armour plate steels and their effects on the microstructure and mechanical properties.

Element	Effect	Proposed specification
C	High C content increases the volume fraction of retained austenite after quenching to martensite. Increases the micro-hardness of the martensite	0.38% - 0.45%
Mn	Improves the hardenability of the steel. Weak carbide former.	0.50% - 2.0 %
Mo	Only the metastable Mo_2C provides secondary peak hardening by tempering at about 500^0C. Mo_2C forms by separate nucleation on dislocations. $M_3C \rightarrow Mo_2C \rightarrow M_6C$ At 700°C, Mo_2C dissolves and transforms to M_6C. [72, 77] (this will also happen at lower temperatures, such as 600 and 650ºC)	Not applicable in this case 0.6% maximum
Ni	Solid solution hardening. Increases the precipitate/matrix misfit by modifying the lattice spacing of the matrix. Grain refiner, decreases the DBTT. Has a strong effect on decreasing the A_{C1} .	2% - 4.0%
Cr	Cr is effective in retarding the softening from Fe_3C in tempering by forming M_3C. M_7C_3 has little strengthening effect.	1.5 %
Cu	Increases the matrix precipitation of Cu, apparently due to a heterogeneous nucleation mechanism on vacancy-Cu atom combinations [74].	0.3%
Si	Reduces the lattice spacing of the ferritic matrix and increases the precipitate/matrix misfit. Delays the decomposition of the martensite and the precipitation of the transition carbides upon tempering. Increases the corrosion resistance.	1.2% maximum
P	Segregates to grain boundaries	Unwanted in this case and must be reduced to lower than 0.005%P
S	Segregates to grain boundaries	Unwanted.
N	Increases the hardenability, decreases the M_s temperature and forms coarse carbonitrides	Unwanted

To move from the current steels A, B, C and D to the high performance steel armour plates by changes only to the heat treatment parameters, e.g. the solution treatment temperature, the temperature of the last pass in the rolling mill, the cooling rate after rolling, the tempering temperature and time, could be considered as the first approach to the objective.

Changes to the chemical composition of an improved alloy would be considered later if the changes to the thermomechanical parameters are not sufficient for achieving the required properties. It is likely, however, that the harder and tougher armour plate will require a change in composition for achieving its hardness, hardenability as well as its toughness.

3.3. The Heat treatment design

The Grossman hardenability of the current steels A and B alloy is about 33 mm. This is sufficient for producing a fully martensitic microstructure through the entire thickness of a 6 mm thick plate. Nevertheless, the true mass fraction of martensite formed at the centre of the plate will be strongly dependent on the cooling rate and the initial temperature before quenching. The final hardness, toughness and strength will depend on all of the parameters considered at each step of the thermomechanical treatment.

The Carbon equivalent is not a highly accurate parameter for predicting the weldability but it nevertheless allows a first qualitative assessment. For good weldability, the Carbon Equivalent (CE) should be less than 0.6%. Above CE = 0.6%, there is a risk of forming martensite and weld-cracking may occur [2]. For armoured steels, it will certainly be difficult to simultaneously obtain good mechanical properties together with good weldability, because the Carbon content cannot be decreased to lower values without compromising the hardness. The high CE, however, does not mean that welding is impossible. Specific pre- and post-treatment of the steel should be adopted to avoid any damage after welding.

The ballistic performance of these alloys will depend on the ability to form a homogeneous martensitic microstructure throughout the cross section of the plate. The Cr-containing carbide M_3C and the additions of Cr to a ferritic low Carbon steel will delay the onset of overageing or softening considerably [73]. The hardening precipitates should be formed within the matrix or on dislocations, and not on grain boundaries. For this, the driving force for precipitation must be high enough and the precipitates as fine as possible for an effective pinning of dislocations and grain boundaries.

From the above considerations the heat treatment cycle for the armoured steels may comprise:

- Solution treatment for homogenisation at 1050 - $1100\,^{0}C$ for 1 hr;
- Hot rolling with the temperature during the last pass in the rolling mill between A_{c3} + 50 to $+100\,^{0}C$ according to the chemical composition. Using the lowest possible finishing temperature for hot rolling of plates is also beneficial for grain refinement but it can be detrimental to the shape and the surface finish of the plate and of the Manganese sulphide particles [72];
- The degree of the hot work will be between 20% and 30% strain per pass;
- Air-cooling to room temperature;
- Austenitisation at $800\,^{0}C$ to $950\,^{0}C$ for 1 hour;

- Water-quenching to room temperature;
- Tempering (for stress relief and precipitation) at 150^0C to 300^0C for less than 1hour. The particular tempered structure should produce the best combination of strength, resistance to spalling and to localised yielding;
- Air-cooling

3.4. Experimental Variables

To optimise the mechanical properties of the armoured steel plates the following variables have been considered:

1. The chemical composition is considered to be the primary independent variable of the system. It has a determining influence on the martensite start temperature, the volume fraction of retained austenite, the type as well as the thermodynamics, kinetics and the nucleation sites of precipitation during tempering. These factors may determine the mechanical behaviour of the armoured steel plates. Four armoured steels, namely Steel A, Steel B, Steel C and Steel D were used for the preliminary investigation of the effect of the chemical composition on the microstructure, mechanical and ballistic performances. Thereafter nineteen laboratory cast steels with carefully chosen chemical compositions have been tested in two steps. First, steels E through to I, and later after their ballistic testing, Steels J through to W have been tested. The chemical compositions of these twenty-three armoured plate steels are presented in tables (3.2) and (4.3.32).

2. The martensite start temperatures of the steels are strongly dependent on their chemical compositions, but are also functions of the austenitisation temperature and time, which determine the degree of carbide dissolution, the grain size and the grain boundary surface area per unit volume. Moreover the martensite start temperature of the steel determines the morphology of the martensite, either plate or lath martensite, and the volume fraction of retained austenite, which influence the mechanical properties as well as the ballistic performance of the plates. The martensite start temperatures of the twenty-three armoured steels have been measured and an empirical relationship with the chemical composition is proposed for these steels using a multilinear regression method. The surface relief after the martensitic transformation was measured by Atomic Force Microscopy (AFM) and the results are compared between the alloys with low M_s and those with high M_s temperatures. The defect structures in the martensite/retained austenite microstructures are also compared between the different alloys.

3. The austenitisation temperature and time determine the grain size, the degree of carbide dissolution into the matrix and, therefore, the martensite start temperature of the alloys. Four austenitisation temperatures ranging from 800^0C to 950^0C were selected for this purpose. The minimum temperature of 800^0C is based on the measurement of the austenite finish temperature, which was found to be between 739^0C and 768^0C for the twenty-three steels. A minimum austenitisation temperature of ($A_f + 50^0C$) has been considered which is approximately 800^0C. The maximum of 950^0C has been chosen to avoid the disadvantages of coarse austenite grains.

4. The Reheat-quench versus Direct-quench (i.e. directly quenched from hot rolling) effect on the ballistic performance has also been investigated. Plates from five alloys were reheated at 900^0C before being water quenched. Plates from eight other alloys were directly water quenched after the final hot rolling pass in the laboratory hot rolling mill. The effect of a second reheating of the armoured steel plates for 15 minutes at 850^0C after the first ballistic testing have also been investigated on plates from five alloys.

5. The location and shape of the retained austenite in the inter-lath or inter-martensite plate spaces may influence the plastic behaviour of the armoured steel plates. Its effects on the ratio between the yield strength and the ultimate tensile strength of seven alloys have been measured and the effects on the diameter of the deformed regions after the ballistic testing were analysed on eight alloys.

6. The tempering temperature and time may strongly affect the existence and properties of the martensitic armoured steels. The effect of low-temperature tempering treatments on the carbide precipitation behaviour and on the mechanical properties and ballistic performance of the alloys have been analysed. The hardness, the tensile properties, the Charpy V impact energy at -40^0C, the precipitation following different tempering conditions, were also compared for the different alloys. The crack formation and the spalling of the plate due to high velocity impacts during the ballistic testing were compared for the different tempering conditions.

7. The lattice parameters of the martensite and the austenite, and their orientation relationships were measured and compared to the predicted values calculated through the phenomenological theory of the martensitic transformation. An approach based on the Bowles and Mackenzie model of the phenomenological theory of the martensite transformation for the calculation of the transformation characteristics and their relationships with the ballistic performances, was examined. A MATLAB script of the BM model is presented for the calculations. The lattice parameters are functions of the chemical composition of the steel and the temperature of the quenching medium. Therefore, they should be considered as dependent variables and their dependencies on the first variables always considered during the analysis.

8. The plate thicknesses through hot rolling have been varied between 4.7 mm and 6.2 mm and the effect of this was compared in terms of radius of the affected region due to the high velocity impact with the fired rounds, the subsequent work hardening and the resistance to cracking and spalling.

Table (3.2): Chemical composition (wt%) of armour steels currently produced or used in RSA and elsewhere in the World

	C	Mn	P	S	Si	Cu	Ni	Cr	Mo	V	Nb	Ti	*N*
Steel A	0.37	0.52	0.005	0.002	0.754	0.855	3.8	0.318	0.367	0.003	0.001	0.003	
Steel B	0.317	0.855	0.008	0.002	0.176	0.26	2.8	0.79	0.45	0.005	0.001	0.003	0.009
Steel C	0.37	0.684	0.003	0.002	0.241	0.005	1.9	0.48	0.32	0.004	0.001	0.003	0.009
Steel D	0.385	0.55	0.004	0.002	0.768	0.1	1.79	0.14	0.36	0.001	NIL	0.007	

3.5. Plate manufacturing

In addition to the four alloys already available at the start of the investigation, nineteen further chemical compositions were designed for the armoured steel plates to be tested. The main raw material, about 5 kilograms of steel B for each melt, supplied by Mittal Steel South Africa, was melted in an alumina crucible of a vacuum induction furnace under argon with an appropriate addition of high grade ferromanganese to adjust the chemical composition to the target. The melted material was degassed. The alloys were cast into a 45 mm x 70 mm x 230 mm mild steel mould. The final compositions of the cast ingots were verified by spectrometer analysis. The top and bottom of the slabs were cut off to remove the casting defects and the final lengths of the slabs were about 190 mm. The ingots were processed by hot rolling with a 20% strain per pass maximum. The first passes in the rolling mill were with the rolling direction parallel to the 70 mm long side to be elongated up to about 200 mm. The sheet was reheated to 950°C for 20 minutes and hot rolled this time with the rolling direction parallel to the 230 mm long side. This second reduction is referred to as the rolling direction in the next Sections of this work.

The slabs were solution treated for one hour at 1100°C before hot rolling. The temperature of the slab at the last pass in the rolling mill was between $900^{0}C$ and $950^{0}C$ with a 20% thickness reduction per pass. After reduction to the desired thickness the plates were air-cooled. The final thickness of the plate was considered as a variable in the study of the ballistic performance. The smallest selected thickness was 4.7mm and the highest was 6.2mm. The plate's sizes for ballistic testing after hot rolling were 200 mm to 250 mm wide and 500 to 550 mm in length. Two or three plates were obtained from each of the nineteen chemical compositions. One plate from each alloy was used for the determination of the mechanical properties and a second for the ballistic testing.

3.6. Mechanical testing

The shock between the fired round and the armoured plate is a high strain rate deformation process. The localised temperature within the shock waves of the impacted region may rise by some hundreds of degrees Celsius [18] due to the conversion of a part of the kinetic energy of the fired round into heat. Another fraction of the kinetic energy is adsorbed by the mechanical strain around the impact region and a third fraction is dissipated through the supports of the structure holding the plate.

The interaction between the plate and the fired round is complex, however, and the following mechanical properties have been suggested for predicting the ballistic performance of steel armoured plates [1,2,6,8,12,15,18]:

- the hardness of the steel at room temperature;
- the tensile strength at room temperature;
- the elongation during tensile testing at room temperature; and
- the Charpy impact energy at $-40^{0}C$.

These mechanical properties were measured for seven steels selected from amongst the twenty-three steels considered in the study. The hardness measurement, the dilatometer analysis and X-Ray diffraction results were considered as a basis for the selection of the seven steels.

The hardness of the plates after hot rolling and air-cooling was higher than 500 Vickers. They were then annealed and furnace cooled before the manufacture of the specimens for tensile and Charpy V impact testing.

The samples were then austenitised for 20 minutes at 800^0C, 850^0C, 900^0C and 950^0C respectively in an Argon atmosphere to prevent oxidation of the steels. The furnace used was LINDBERG MK-1018 with maximum temperature of 1200^0C. After austenitisation, the samples were water quenched to 20^0C to form the martensite microstructure. Tempering treatments at 150^0C, 180^0C, 200^0C, 250^0C, 300^0C, 350^0C and 400^0C for times from 15 to 60 minutes, were applied to the alloys.

3.6.1. Hardness measurement

Hitherto the hardness was considered as the main mechanical property for armour plate steels. South African specifications suggest the Brinell hardness to be higher than 600 BHN [1] whereas the American specifications [2] suggest the Rockwell C number to be at least between 55 and 60 Rc for armoured plate. The Australian specifications for military and security applications recommend a Brinell hardness between 478 and 578 BHN. [2]

Four techniques have been used for the measurement of the hardness of the steels in the quenched and tempered conditions, and comparisons have been done with the specifications.

Small samples of the hot rolled plates were cut to 15 mm length and 10 mm width. The thickness varied between 4.7 mm and 6.2 mm depending on the thickness of the plate. Samples were austenitised, quenched and tempered as defined previously and the hardness measured. The samples were finely mounted in resin and mechanically polished before the measurement of the hardness.

The Brinell hardnesses were measured in a hydraulic Otto-Wolpe –Werke machine with a 2.5 mm diameter ball at a constant load of 62.5 kg.

Figure 3.1.The tubular furnace
LINDBERG MK-1018 for austenitisation

The Vickers microhardnesses were measured in a microhardness tester of Future-Tech Corporation of Japan with a load of 300g.

Figure 3.2. Microhardness Tester FM F11-1

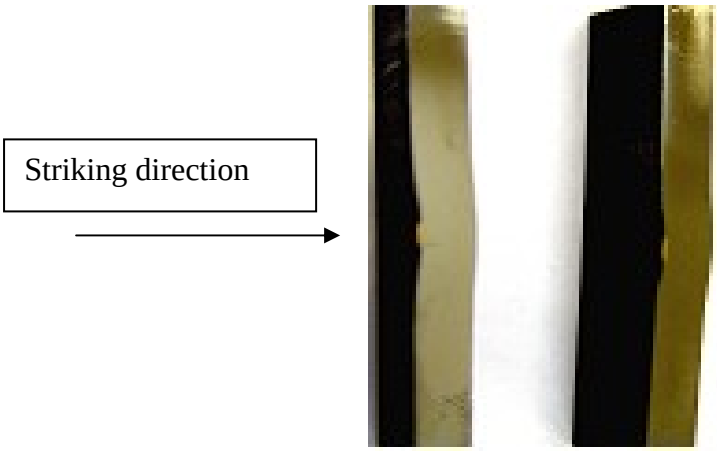

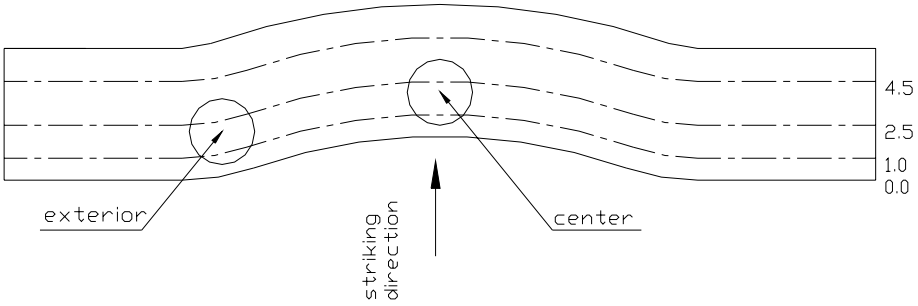

Figure 3.3. (a) Cross sections wire-cut through the ballistic impact-affected regions of steels P and Q. (b) Illustration of the iso-depth lines along which microhardness was measured through the cross sections which were wire cut after ballistic impact.

3.6.2. The tensile strength and elongation

The front surface of the armour plate is subjected to a high rate compressive strain when impacted by a projectile. The rear surface may fail under a high rate tensile stress. Earlier, mention has been made of the localised temperature that rises in the impact region due to shock wave propagation. However, the specifications have been established for ballistic performances using the uniaxial tensile test at room temperature. South African specifications specify the yield strength to be a minimum of 1300 MPa, the tensile strength a minimum of 1700 MPa and the elongation to be more than 7% for good ballistic performance.

The tensile specimens were cut parallel to the rolling direction from the hot-rolled and air-cooled plate for the selected steels. For others, because of a high hardness, an annealing treatment was applied to the plates before the wire cutting of the tensile specimens. The flat tensile specimens had a rectangular cross section calculated according to Barba's law [101] for comparison with the standard specimens.

$$\frac{\sqrt{A_s}}{L_s} = \frac{\sqrt{A_1}}{L_1}$$

where A_s and A_1 are the cross section areas of the standard and the tested specimens respectively and L_s and L_1 their respective gauge lengths. The dimensions of the flat tensile specimens are then:

Table (3.3). Dimensions of the tensile specimens

Total length [mm]	Gauge length [mm]	Accord radius [mm]	Width [mm]	Thickness [mm]
100	33	5	6 ± 0.2	6 ± 0.2

The tensile specimens were wire-cut before the heat treatment to avoid the laborious machining of the hard martensite formed after quenching and were austenitised under Argon, quenched and tempered as stated before. The yield strength, the ultimate tensile strength and the elongation were determined using an INSTRON 8500 hydraulic tensile testing machine.

Figure 3.4. Universal testing machine INSTRON 8500

The Yield strength and the Ultimate tensile strength were correlated through the first constraint equation with the optimum of the hardness and the ballistic performances of the armour steel plates. Fractured specimens were analysed under a scanning electron microscope to establish the mechanisms of fracture and the possible role of inclusions.

3.6.3. The Charpy V-notch impact energy

As in the case of the tensile properties, specifications exist for the impact energy of armoured plate steels. Those specifications utilise the results from a Charpy V-notch test that is relatively a slow strain rate phenomenon compared to the high velocity impact during ballistic testing. The more conservative specifications [2] for armour steels recommend a minimum of 27 Joules impact energy at $-40^{0}C$ on full size Charpy V-notch specimens, which has its axis transverse to the rolling direction. The less conservative specifications [1] fix the minimum at 13 Joules impact energy at $-40^{0}C$ on full size Charpy V specimens with its length normal to the rolling direction. The Impact energy also provides an indication of the resistance of the steels to brittle fracture and to spalling. The resistance to spalling during the impact is a safety criterion and is also a good indication of the ability of the armour steels to absorb the kinetic energy of the bullets. The Charpy-V impact energy of the sub-sized specimens was, therefore, considered as the second constraint on the hardness and the ballistic performance. The relationship between the impact energy and the heat treatment parameters was used to construct the second constraint equation on the optimum level of hardness on ballistic performance.

Because of the plate thicknesses being less than 10 mm, sub-standard Charpy sized specimens had to be used. These were wire-cut with the following dimensions: 55 x 10 x 5 mm. The notch was 2 mm deep with an angle of 45^{0}, and the radius of the fillet at the tip was 0.25 mm.

The Charpy V-notch impact energy of the sub-sized specimens quenched and tempered, were measured at $-40^{0}C$ to construct the second constraint equation on the ballistic performances. Specimens were cooled and kept for 10 minutes at $-60^{0}C$ in a mixture of ethanol and dry ice. They were then heated to $-50^{0}C$ by adding controlled amounts of ethanol to the mixture, and were then removed from the cold liquid and tested. The time between the removal from the cold liquid and the impact of the pendulum was estimated to

be between four and six seconds. Testing was done on a Charpy impact testing machine from Mohr and Federhaff AG, Germany.

Figure 3.5. The Pendulum Impact Testing Machine

3.6.4. Fracture analysis

The fracture surfaces after tensile and impact testing were analysed in a scanning electron microscope to determine the mode of cleavage and the possible role of inclusions in the fracture mechanism. Freshly fractured surfaces were protected against contamination and analysed in the secondary electron mode on a JEOL JSM-6300. Fracture surfaces (if present), cross sections through the impact region, cracks, micro-cracks and grain boundaries in the impact region after ballistic testing were also analysed in both the backscattered and secondary electron modes in the same SEM equipment.

Figure 3.6. Scanning Electron Microscope JEOL JSM-6300, Model P90E.

3.6.5. Microstructure analysis

The microstructure of the steels is the result of a complex combination of the effects of the chemical composition, the mechanical processing and the heat treatment. The properties that determine the ballistic performance of the armour steel plates, may be attributes of the microstructure. The structure and morphology of the martensite laths or plates, the location and volume fraction of retained austenite, its orientation relationships with the martensite and the precipitation of the cementite have been analysed and their effects on the ballistic performances were established. The combination of the scanning electron microscopy, the transmission electron microscopy, the atomic force microscopy and the X-ray diffraction was necessary to fully characterising the microstructures of these armour steels.

3.6.5.1. Phase analysis and Lattice parameters measurements

X-ray diffraction was used to determine the phases present in the steels and their lattice parameters. The analysis was done on two different groups of samples.

The first group was solution treated for 20 minutes at 900^0C in a tubular furnace under an argon atmosphere, water quenched to 20^0C and then electro polished in a solution of 5% volume perchloric acid and 95% volume of glacial acetic acid before the X-ray diffraction analysis. The second group of 1 mm thick discs of the same steels, was finely polished and then solution treated for 10 minutes at 900^0C, under a 10^{-4} torr vacuum in a Theta dilatometer, then quenched to room temperature in Helium gas. The equipment used was from X'Pert PRO PANalytical

Figure 3.7. X-ray diffraction analyser X'Pert PRO PANalytical

3.6.5.2. Morphology of the martensite

The defect structure of the martensitic structure together with the surface relief and the diffusionless character, are proof of the existence of the martensitic transformation. The Bright Field and Dark Field Images from the TEM were analysed to determine the morphology of the plate or lath martensite, and the phases present such as the retained austenite and the cementite. Carbon replicas and thin foils of fifteen armour steels were analysed.

The thin foils were prepared from the 3 mm diameter discs wire-cut as shown in Figure 3.4 in the as-quenched or in the quenched and tempered plates before and after ballistic impact. The discs had an initial 0.6 mm thickness. They were mechanically polished to less than 200 micrometers in thickness before eletropolishing in a solution of 6vol% of perchloric acid and 0.5vol% chromium oxide in glacial acetic acid. The thin foils and the carbon replicas were analysed in a PHILIPS CM 200 TEM equipped with STEM, EDS and an electron beam source of 160 kV.

Figure 3.8. Transmission Electron Microscope PHILIPS CM 200

3.6.6. Transformation surface relief

The surface relief after the martensitic transformation was measured on a nanometre scale using the Atomic Force Microscope Topometrix TMX 2000 "Discoverer". The samples for the atomic force microscopy were prepared from 1 mm thick specimens of the selected steels. They were finely polished on a one micron diamond paste before electropolishing in a solution of 5vol% perchloric acid and 95vol% glacial acetic acid at 0ºC. The polished samples were then austenitised for 10 minutes at $900^{0}C$ under high vacuum in the Theta dilatometer and quenched to room temperature in a flow of Helium gas. The quenched samples were then cleaned in an ultrasonic cell with pure acetone to remove any contamination or dust from the surface.

The very small features such as the size of the twins, the twinning angles and the relative orientation between the plate axis and the twins were measured for these steels. The Fast Fourier Transform implemented by the discrete Fourier transform algorithm was used to analyse the periodicity of the surface relief. The calculations were performed using MATLAB 7.0 software.

Figure 3.9. Atomic Force Microscope: Topometrix TMX 2000 "Discoverer"

3.7. Martensite start temperatures

The characteristic transformation temperatures during cooling of all twenty-three steels were measured by a dilatometer. The Martensite start temperatures were correlated with the chemical compositions and with the solution treatment temperatures of all 23 steels and an empirical relationship is proposed for estimating the M_s temperature of these armour steels. The M_s temperature was used later as an indirect variable for estimating the volume fraction of retained austenite in the martensitic steel and the orientation relationship between the retained austenite and the martensite. The dependence of the ballistic performances of these armour plate steels on the M_s temperature were also analysed. The autotempering phenomenon was also detected for some of these steels through the dilatometer curves.

The sample preparation for the dilatometer analysis is described in paragraph 3.6.5.1. The equipment used was a THETA 734 Single Silica Push Rod LVDT dilatometer.

Figure 3.10. Dilatometer THETA 734

3.8. Ballistic testing

3.8.1. Specifications for the test

Thirteen armoured steels were tested in a ballistic testing tunnel at Mittal Steel South Africa (Vanderbijlpark) where the temperature and the humidity are controlled as specified, to standardise testing conditions. The testing distance was 30 metres and the obliquity angle was zero degrees. One plate was tested from a distance of only 10 meters. The prescribed velocity range for the R4's 5.56 mm rounds is 940 ± 10 m/s. An optical testing system assesses the success or failure of the plate by remaining opaque to a light beam.

3.8.2. Analysis after ballistic testing

After ballistic testing optical and scanning electron microscopy analyses were done on the front and rear surfaces of the plates. The impact region was sectioned by wire cutting and a cross section was analysed through optical and scanning electron microscopy for crack analysis. Hardness profiles along three iso-depth lines, respectively at 1.5, 2.5 and 4.5 mm

below the front surface of the impact region, were determined. Finally thin foils from the centre and the periphery of the impact region were analysed by TEM and their microstructures compared to the initial martensite before ballistic testing.